AGU PUBLICATIONS

JGR

Journal of Geophysical Research: Solid Earth

RESEARCH ARTICLE
10.1002/2015JB012429

Key Points:
- First azimuthal anisotropy model in oceanic lithosphere/asthenosphere from array analysis of OBSs
- Flow in lithosphere was not perpendicular to spreading axes but was parallel to ancient plate motion
- Combination of surface wave and shear wave splitting implied depth extent of azimuthal anisotropy

Correspondence to:
A. Takeo,
akiko-t@eri.u-tokyo.ac.jp

Citation:
Takeo, A., H. Kawakatsu, T. Isse, K. Nishida, H. Sugioka, A. Ito, H. Shiobara, and D. Suetsugu (2016), Seismic azimuthal anisotropy in the oceanic lithosphere and asthenosphere from broadband surface wave analysis of OBS array records at 60 Ma seafloor, *J. Geophys. Res. Solid Earth*, *121*, 1927–1947, doi:10.1002/2015JB012429.

Received 20 AUG 2015
Accepted 2 MAR 2016
Accepted article online 6 MAR 2016
Published online 30 MAR 2016

Seismic azimuthal anisotropy in the oceanic lithosphere and asthenosphere from broadband surface wave analysis of OBS array records at 60 Ma seafloor

A. Takeo[1], H. Kawakatsu[1], T. Isse[1], K. Nishida[1], H. Sugioka[2,3], A. Ito[3], H. Shiobara[1], and D. Suetsugu[3]

[1]Earthquake Research Institute, University of Tokyo, Tokyo, Japan, [2]Department of Planetology, Kobe University, Hyogo, Japan, [3]Department of Deep Earth Structure and Dynamics Research, Japan Agency for Marine-Earth Science and Technology, Kanagawa, Japan

Abstract We analyzed seismic ambient noise and teleseismic waveforms of nine broadband ocean bottom seismometers deployed at a 60 Ma seafloor in the southeastward of Tahiti island, the South Pacific, by the Tomographic Investigation by seafloor ARray Experiment for the Society hotspot project. We first obtained one-dimensional shear wave velocity model beneath the array from average phase velocities of Rayleigh waves at a broadband period range of 5–200 s. The obtained model shows a large velocity reduction at depths between 40 and 80 km, where the lithosphere-asthenosphere boundary might exist. We then estimated shear wave azimuthal anisotropy at depths of 20–100 km by measuring azimuthal dependence of phase velocities of Rayleigh waves. The obtained model shows peak-to-peak intensity of the azimuthal anisotropy of 2%–4% with the fastest azimuth of NW–SE direction both in the lithosphere and asthenosphere. This result suggests that the ancient flow frozen in the lithosphere is not perpendicular to the strike of the ancient mid-ocean ridge but is roughly parallel to the ancient plate motion at depths of 20–60 km. The fastest azimuths in the current asthenosphere are subparallel to current plate motion at depths of 60–100 km. Additional shear wave splitting analysis revealed possible perturbations of flow in the mantle by the hot spot activities and implied the presence of azimuthal anisotropy in the asthenosphere down to a depth of 190–210 km.

1. Introduction

The deformation in the uppermost mantle causes lattice preferred orientation (LPO) of mantle minerals. For the case of olivine crystals, the dominant constituent of the upper mantle, the LPO provides strong azimuthal anisotropy with the fastest axis parallel to the direction of flow [*Hess*, 1964; *Francis*, 1969]. Such anisotropy has been determined by refraction surveys [e.g., *Raitt et al.*, 1969] and surface wave studies [e.g., *Tanimoto and Anderson*, 1984]. The surface wave studies have also determined the radial anisotropy, the discrepancy between velocities of vertically and horizontally polarized *S* waves (V_{SV} and V_{SH}), by using two types of surface waves, Rayleigh and Love waves [*Aki and Kaminuma*, 1963; *Forsyth*, 1975].

Recent surface wave tomography studies have determined mantle models including radial anisotropy [e.g., *Nettles and Dziewonski*, 2008; *French et al.*, 2013], azimuthal anisotropy [e.g., *Montagner*, 2002; *Debayle and Ricard*, 2013], and low-velocity zone (LVZ) at depths of ~50–200 km [e.g., *Maggi et al.*, 2006a]. Since the LVZ and the overlying high-velocity lid most likely correspond to the oceanic asthenosphere and lithosphere [*Revenaugh and Jordan*, 1991; *Kawakatsu et al.*, 2009], the oceanic structure including lid, LVZ, and anisotropy is essential to understand the flow in the uppermost mantle related to motions of oceanic plates. Some parts of the structure are, however, difficult to determine as described below.

One difficulty is to determine structure in the lid. The refraction survey mainly has resolution to the top ~10 km of the uppermost mantle. The depth range is not sufficient to image the entire lid, although the isotropic velocity at deeper depths can be somewhat resolved by taking account into both arrival times and amplitudes of Pn waves [*Lizarralde et al.*, 2004; *Gaherty et al.*, 2004]. On the other hand, surface waves at periods shorter than ~30 s have resolution to the lid. Since the wavefield is usually complicated owing to the strong

heterogeneity at shallow part, we need to analyze array records of ocean bottom seismometers (OBSs) by methods such as the array analysis of teleseismic surface waves [*Forsyth and Li*, 2005] and the ambient noise cross-correlation analysis [*Harmon et al.*, 2007]. We can then obtain the vertical structure from the crust to the top of the asthenosphere [*Harmon et al.*, 2007; *Yao et al.*, 2011] including radial anisotropy [*Takeo et al.*, 2013].

Another difficulty is to obtain the absolute intensity of seismic anisotropy. Many previous studies have constructed mantle anisotropic models using surface waves [*Smith et al.*, 2004; *Maggi et al.*, 2006b; *Debayle and Ricard*, 2013; *Yuan and Beghein*, 2013; *Burgos et al.*, 2014]. For the tomography analysis, however, the intensity of anisotropy depends on the assumed smoothing or damping parameters especially when the heterogeneity of azimuthal anisotropy is large such as in the lid [*Smith et al.*, 2004]. To estimate the intensity, we need to observe the azimuthal dependence of velocity as done by refraction surveys [*Raitt et al.*, 1969] or by surface wave array analysis in continental region [*Alvizuri and Tanimoto*, 2011].

Those difficulties have hampered parts of discussion and inferences of previous studies such as the difference between the causes of seismic anisotropy in the lithosphere and asthenosphere. We need to improve the vertical and lateral resolutions of azimuthal anisotropy to discuss the cause of seismic anisotropy and finally deformation process in the uppermost mantle.

In this study, we focus on isotropic and azimuthally anisotropic V_{SV} at a depth range of 10–150 km by analyzing Rayleigh waves at periods of 5–200 s from the seafloor records in the French Polynesia region. Although radial anisotropy could not be determined due to the possible interference between fundamental and first higher modes of Love waves (section 6.5), the azimuthally anisotropic model still has enough resolution to provide new insights into the oceanic lithosphere and asthenosphere system in the local study area, which was difficult either by the early surface wave studies in 1970–1980s or by recent tomography studies.

2. Study Area and Data

The data used in this study are the three-component records of nine broadband ocean bottom seismometers (BBOBSs) [*Suetsugu and Shiobara*, 2014] deployed at the southeast of Tahiti Island in the French Polynesia region, south Pacific Ocean, by the Tomographic Investigation by seafloor ARray Experiment for the Society hotspot (TIARES) project [*Suetsugu et al.*, 2012]. The French Polynesia region is characterized by hot spot islands inside the Pacific Superswell region [*McNutt*, 1998; *Adam and Bonneville*, 2005]. *Duncan and McDougall* [1976] determined the ages of hot spot islands and revealed their movements after ~10 Ma. The direction of motion is parallel to the present-day plate motion (HS3-NUVEL-1) [*Gripp and Gordon*, 2002]. *Schlanger et al.* [1984] determined the movement of older hot spot islands from the youngest Tuamotu islands (~45 Ma) to the north (~90 Ma). The direction of motion is subparallel to the present-day plate motion, reflecting the change in the motion of Pacific Plate at ~43 Ma [*Lonsdale*, 1988].

The BBOBS observation in this region was first conducted from 2003 to 2005 as a Japan-France cooperative project [*Suetsugu et al.*, 2005] in order to cover the gap in seafloor region remained by another project on the hot spot islands, the PLUME project [*Barruol*, 2002]. These projects revealed roots of hot spots by the local surface wave tomography [*Isse et al.*, 2006; *Maggi et al.*, 2006a, 2006b], flow in the mantle by the shear wave splitting analysis [*Barruol et al.*, 2009], the structure of the mantle transition zone by a receiver-function analysis, and the lower mantle by body wave tomography and receiver-function analysis [*Suetsugu et al.*, 2009]. The typical interstation distance of the project was ~500 km and was too large for the surface wave study at periods shorter than 30 s.

Nine BBOBSs were later deployed more densely from February 2009 to July 2010 as a part of TIARES project [*Suetsugu et al.*, 2012] to reveal the mantle structure beneath the Society hot spot, whose volcanic activity formed the Society islands. The observation area (Figure 1) is not above the active hot spot itself but at the nearby seafloor in an effort to image the root of hot spot from the lower mantle. The area, thus, lacks lateral heterogeneity compared to surrounding regions [*Isse et al.*, 2006] and is suitable for this study to obtain structure within the oceanic lithosphere and asthenosphere. In this study, we basically investigate one-dimensional structure beneath the array of BBOBSs and additionally discuss the lateral variation. The average seafloor age is 60 Ma and is older than the seafloor ages of 0–20 Ma for previous array analysis of BBOBSs [*Harmon et al.*, 2007; *Yao et al.*, 2011; *Takeo et al.*, 2013].

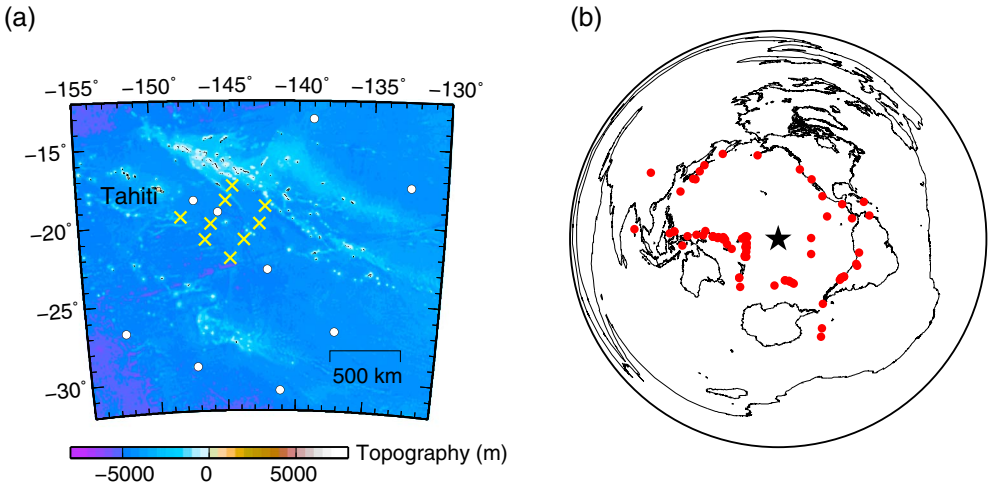

Figure 1. (a) Map showing nine BBOBS stations of the TIARES project (yellow crosses) and seafloor stations of previous project (white circles) in the French Polynesia region. (b) Red circles show the epicenters of teleseismic events used in this study. Star shows the location of the BBOBS array by the TIARES project.

3. Average Phase Velocities and 1-D Isotropic Model

The broadband analysis of surface waves at periods of ~5–200 s is essential for obtaining uppermost mantle structure from the crust to a depth of ~150 km. We first used the ambient noise cross-correlation method to analyze surface waves at periods of 5–30 s and used the teleseismic surface waves at periods of 30–200 s. In each analysis, we measured azimuthally and spatially averaged phase velocities of Rayleigh waves to determine one-dimensional shear wave velocity model beneath the array of nine stations.

3.1. Ambient Noise Cross-Correlation Analysis

At periods shorter than 30 s, we extracted the background surface wave propagation between pairs of stations by cross-correlating continuous records of ambient noise. We here use the method developed by *Takeo et al.* [2014], which is based on the method by *Aki* [1957]. We first calculated cross-correlation functions (CCFs) between every pair of stations and components by calculating the cross spectra in the frequency domain and by taking the inverse Fourier transform. The cross spectrum is defined as

$$S_{ij}^{kl}(\omega) = \frac{\langle W_{ij}^{kl}(\omega) \cdot (F_i^k(\omega))^* \cdot F_j^l(\omega) \rangle}{\langle W_{ij}^{kl}(\omega) \rangle}, \tag{1}$$

where $\langle\ \rangle$ means the ensemble average, ω is angular frequency, and F_i^k is a Fourier spectrum of the component k record at the ith station with a time window of 2621.44 s. Each time window is half overlapped with the adjacent time windows. For discarding earthquake signals automatically, we calculated mean power at 0.03 Hz for each time window and discarded any time window whose amplitude exceeds 10 times of the amplitude for the previous time window. With this criterion, 10%–20% of time windows were discarded for each station and component. The weighting term is given by $W_{ij}^{kl}(\omega) = |\tilde{F}_i^k(\omega)|^{-1} \cdot |\tilde{F}_j^l(\omega)|^{-1}$. The normalized amplitude is $|\tilde{F}_i^Z| = |F_i^Z|$ for the vertical component, and $|\tilde{F}_i^T| = |\tilde{F}_i^R| = \sqrt{(|F_i^T|^2 + |F_i^R|^2)/2}$ for the two horizontal components. The uncertainty of calculated cross spectrum is given by $\langle W_{ij}^{kl} \rangle^{-1} \mathcal{O}\left(N^{-1/2}\right)$, where N is the number of ensembles [*Takeo et al.*, 2013, Appendix A].

Figures 2 shows CCFs obtained by the inverse Fourier transformation of the cross spectra calculated from the vertical ($k = l = Z$, ZZ component), radial (RR), and transverse (TT) components of BBOBS records. The ZZ and RR component CCFs show the propagation of the fundamental mode Rayleigh wave (0S mode) and the first higher-mode Rayleigh wave (1S mode), whereas the TT-component CCFs show the propagation of the Love wave (xT mode). The mode of Love wave could not be identified due to possible interference between the fundamental mode and the higher mode with very similar group and phase velocities (see more detail in section 6.5). We excluded the ZZ component CCFs for three pairs from the figure and the analysis because they showed anomalous signal in addition to the 0S and 1S modes. The anomalous signal seems to reflect correlations between hourly mechanical noise in the raw records.

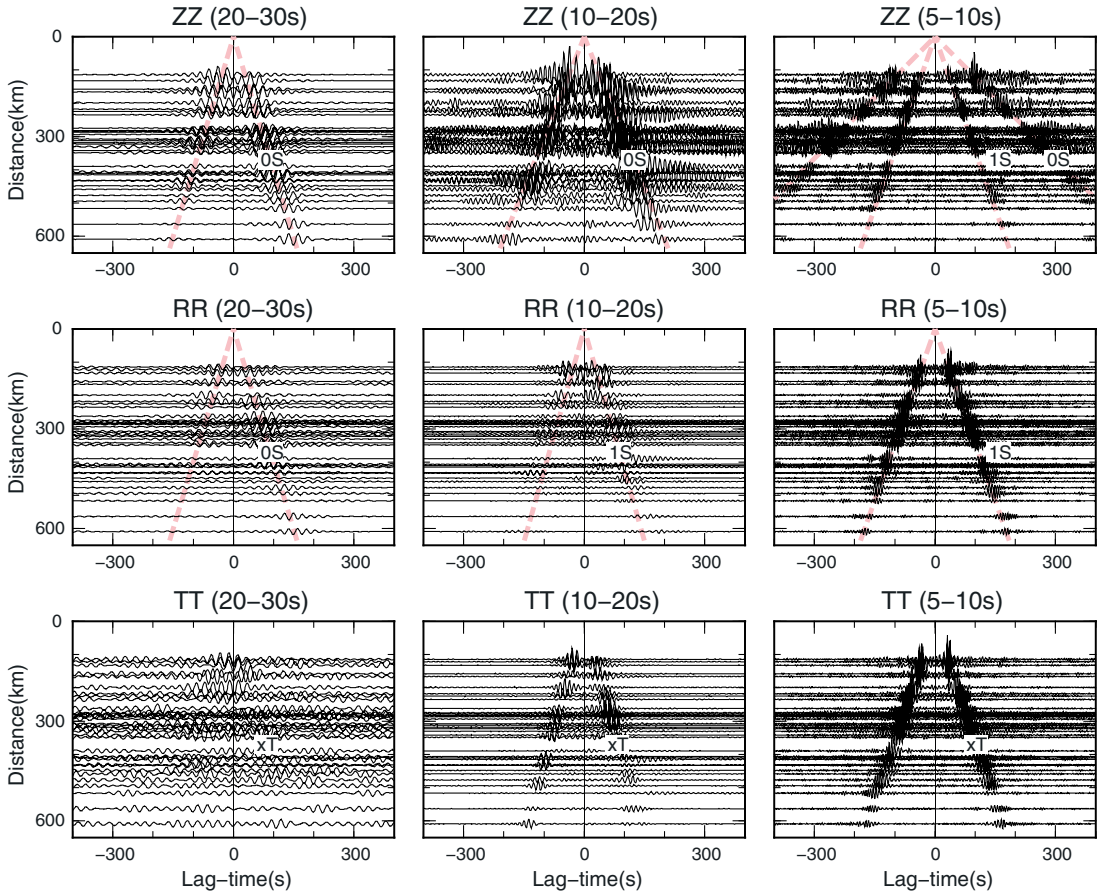

Figure 2. Cross correlation functions as function of interstation distances filtered at 20–30 s, 10–20 s, and 5–10 s. The amplitudes are multiplied by $\langle W_{ij}^{kl} \rangle$ in the frequency domain to produce similar noise levels for different pairs of stations. Dashed pink line shows the group velocity of each specified mode at a typical period for our one-dimensional isotropic model shown in Figure 3b. The modes include the fundamental mode and first higher-mode Rayleigh waves, 0*S* and 1*S*. The *TT* components show an unknown mode of Love wave, *xT*.

We then searched average phase velocities and average amplitudes of multimode Rayleigh waves. The model parameters are phase velocity (c_m) and amplitude (a_m^{kl}) of each mode (m) in each component (k, l) at each angular frequency (ω). According to the equation by *Aki* [1957], the synthetic cross spectra, $S_{ij}^{\prime kl}$, are given by

$$S_{ij}^{\prime ZZ} = a_{0S}^{ZZ} J_0\left(\frac{\omega d_{ij}}{c_{0S}}\right) + a_{1S}^{ZZ} J_0\left(\frac{\omega d_{ij}}{c_{1S}}\right),$$
$$S_{ij}^{\prime RR} = a_{0S}^{RR} J_{0-2}\left(\frac{\omega d_{ij}}{c_{0S}}\right) + a_{1S}^{RR} J_{0-2}\left(\frac{\omega d_{ij}}{c_{1S}}\right), \quad (2)$$

where d_{ij} is the distance between the ith and the jth stations, J_n is the nth Bessel function of the first kind, $J_{0-2}(x) = J_0(x) - J_2(x)$. We expressed phase velocities of mode m as a summation of B-spline functions, $g_m^n(\omega)$, $c_m(\omega) = \sum_n p_m^n g_m^n(\omega)$, determined the values of coefficients, p_m^n, and minimized the mean square misfit between observed and synthetic cross spectra,

$$L(\mathbf{p}) = \sum_{\omega,kl} \frac{\sum_{ij} \langle W_{ij}^{kl}(\omega) \rangle^2 \left[\Re_e(S_{ij}^{kl}(\omega)) - S_{ij}^{\prime kl}(\omega, \mathbf{p}, \mathbf{a}) \right]^2}{\sum_{ij} \langle W_{ij}^{kl}(\omega) \rangle^2 \left[\Re_e(S_{ij}^{kl}(\omega)) \right]^2}, \quad (3)$$

by the very fast simulated annealing method [*Ingber*, 1989]: We assumed 40,000 combinations of p_m^n, calculated the optimal amplitude of each mode and each component, a_m^{kl}, for each frequency for each assumed combination of p_m^n by the least squares method, and searched for the minimum of the misfit. The unknown

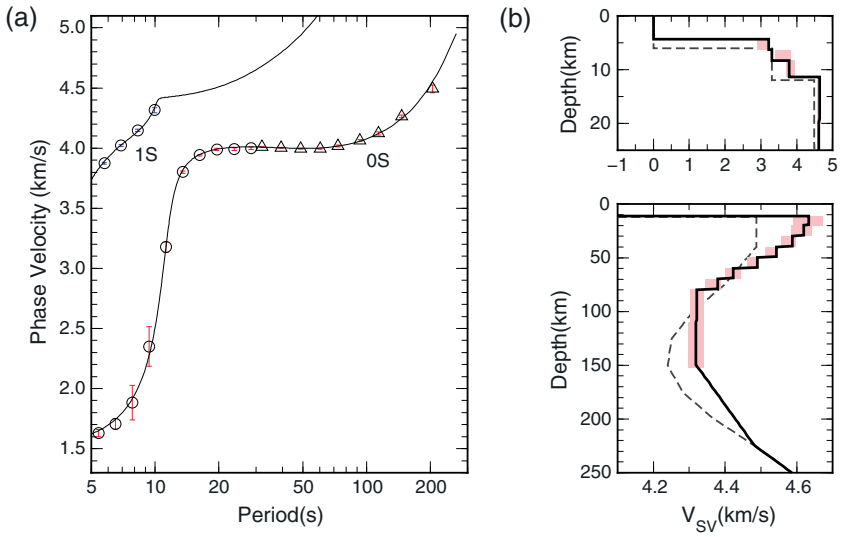

Figure 3. (a) Average phase velocities of Rayleigh waves obtained from ambient noise (circles) and teleseismic waveforms (triangles). The error bars for 0*S* (red) and 1*S* (blue) modes are very small at almost all periods in this scale but have values of 0.004–0.2 km/s. Solid curves are the phase velocities corresponding to a model shown in right figure. (b) Solid line shows one-dimensional smooth V_{SV} model beneath the array of TIARES project for the crustal (Figure 3, top) and mantle (Figure 3, bottom) parts. Pink areas show the uncertainty. The uncertainty of seafloor depth is ±0.04 km, which is not shown in the figure due to small value. Dashed lines shows the ORM model [*Maggi et al.*, 2006a]. The depth of 0 km corresponds to the sea surface.

xT mode can appear in the radial components if the interstation distance is comparable or shorter than the wavelength [*Aki*, 1957]. We neglected the Love wave in radial components because the interstation distances are longer than the wavelength in this study.

The measurement error is estimated using the bootstrap method [*Efron*, 1979], where 100 dispersion curves $(c_m^1(\omega), c_m^2(\omega), \cdots, c_m^{100}(\omega))$ were estimated for each of 100 bootstrap samples. A bootstrap sample is the aggregate of station pairs randomly selected from all station pairs allowing for overlaps. For each component, the number of CCFs in each bootstrap sample is the same as the number of all CCFs. We defined the error of phase velocity measurement $(\Delta c_m(\omega))$ as one standard deviation of 100 dispersion curves. Figure 3a shows the optimal phase velocity curve and the error range $(\bar{c}_m(\omega) \pm \Delta c_m(\omega))$, where $\bar{c}_m(\omega)$ is the average value taken from the 100 dispersion curves.

The period range of precise phase velocity measurements is limited to 5–10 s for the 1*S* mode and 5–30 s for the 0*S* mode. At shorter periods, the signal may be difficult to extract because of lateral heterogeneity in the crust. At longer periods, the signal-to-noise ratio of CCFs is low due to high noise levels of BBOBSs (see typical noise level of BBOBS in *Suetsugu and Shiobara* [2014]).

3.2. Teleseismic Event Array Analysis

At periods longer than 30 s, the phase velocities of Rayleigh waves were measured by using vertical components of teleseismic events with moment magnitudes larger than M_w 5.5, focal depths shallower than 200 km, and great circle distances greater than 3000 km. We first estimated a back azimuth for each event to eliminate the effect of ray bending from the phase velocity measurements [*Forsyth and Li*, 2005]. We then measured average phase velocities by using all the events simultaneously [*Takeo et al.*, 2013].

The first step estimates the phase velocity $(c_E = \sum_n p_E^n g^n(\omega))$ and the perturbation of incident direction from the great circle $(\theta_E = \sum_n q_E^n g^n(\omega))$ for each event (E) by maximizing the average of cross-correlation coefficients (C_E) defined as

$$C_E(\mathbf{p}, \mathbf{q}) = \frac{1}{N_E} \sum_{i,j} \frac{\sum_\omega \Re_e \left[F_i \cdot (F_j)^* \cdot e^{i\Delta\varphi_{ij}(\omega, c_E, \theta_E)} \right]}{\sqrt{\sum_\omega |F_i|^2} \sqrt{\sum_\omega |F_j|^2}}, \tag{4}$$

where $F_i(\omega)$ is the Fourier spectrum of the ith station, N_E is the number of station pairs, and $g^n(\omega)$ is a nth B-spline function. The phase difference between the ith and jth stations, $\Delta\varphi_{ij}$, is estimated by assuming a propagation of one plane wave in local coordinates [*Forsyth and Li*, 2005]. Using equation (4), we obtained the optimal phase velocity and incident direction for each event by the simulated annealing method [*Ingber*, 1989]. The next step uses events whose average cross-correlation coefficient ($C_E\left(\mathbf{p}_E, \mathbf{q}_E\right)$) larger than 0.7.

In the second step, we searched for the optimal phase velocity curve ($c(\omega)=\sum_n p^n g^n(\omega)$) that maximizes the summation of cross-correlation coefficients for each mode,

$$C(\mathbf{p}) = \sum_E N_E C_E\left(\mathbf{p}, \mathbf{q}_E\right), \tag{5}$$

where the incident direction is fixed by the optimal value for each event ($\theta_E = \sum_n q_E^n g^n(\omega)$) obtained in the first step. Figure 3a shows phase velocities of 0*S* mode at periods of 30–200 s. The number of available events was 81 as the epicenters shown in Figure 1b. Figure 3a also shows the range of errors estimated by the bootstrap method [*Efron*, 1979], where a bootstrap sample was constructed using a randomly selected aggregate of events that were allowed overlaps. The phase velocity at a period of about 30 s is consistent with that determined by the noise correlation analysis.

3.3. 1-D Isotropic Model

The phase velocities of Rayleigh waves measured in this study mainly reflect shear wave velocity (V_S) from the crust to a depth of ~150 km. In addition, phase velocities of Rayleigh waves at periods of 10–20 s reflect depth of the ocean. We therefore estimated isotropic V_S in each of nine layers from the Moho to a depth of 150 km, isotropic V_S in each of three layers in the crust with a total thickness of 7 km, and the seafloor depth. Since Rayleigh waves mainly reflect V_{SV} [*Takeuchi and Saito*, 1972], the isotropic V_S of obtained model also reflects V_{SV}. The detail of assumptions for the crustal structure is as same as those well described in *Takeo et al.* [2013]: (i) *P* wave velocity (V_P) in the mantle is constrained to be 1.73 times larger than V_S. (ii) V_P and density in the crustal layers were scaled via V_S. Other parameters are fixed to the Oceanic Reference Model (ORM) model including mantle density, attenuation coefficients, and structure deeper than 225 km (Figure 3b). The ORM model is an average of three-dimensional tomography model at seafloor ages of 30–70 Ma [*Maggi et al.*, 2006a], which is similar to the PREM model [*Dziewonski and Anderson*, 1981] but has no discontinuity at a depth of 220 km. One layer at a depth range of 150–225 km is set to be linearly connected to the values at depths of 150 and 225 km.

We again used the simulated annealing method to search for optimal model parameters that led to a small misfit function defined by

$$E'_{\mathrm{RA}} = E_{\mathrm{RA}} + \epsilon_{\mathrm{sv}} R_{\mathrm{sv}} \tag{6}$$

$$= \sum_{m,\omega}\left[\frac{\bar{c}_m(\omega) - c_m^{\mathrm{model}}(\omega)}{\Delta c_m(\omega)}\right]^2 \Big/ \sum_m N_m + \epsilon_{\mathrm{sv}} \sum_{i=1}^{N-1}\left(V_{\mathrm{SV}}^{i+1} - V_{\mathrm{SV}}^{i}\right)^2, \tag{7}$$

where N_m is the number of measurements for each mode m and $c_m^{\mathrm{model}}(\omega)$ is the phase velocity calculated by DISPER80 [*Saito*, 1988] using the model parameters. The frequency interval of the measurements is set to be constant on a log scale. The second term is a smoothing term and introduced to reduce the uncertainty related to the trade-off between adjacent layers, where ϵ_{sv} is a constant, V_{SV}^i is V_{SV} in the ith layer, and $N = 9$ is the number of layers.

Figure 3b shows V_{SV} model for the French Polynesia region obtained in this study. *Takeo et al.* [2013] used a smoothing parameter of $\epsilon_{\mathrm{sv}} = 10$ for the Shikoku Basin region. Since the phase velocity measurements of the previous and these studies have similar period ranges and measurements errors, we chose the same smoothing parameter for our inversion. The model gives phase velocities almost consistent with the phase velocity measurements as shown in Figure 3a. We further estimated the model uncertainty by a bootstrap-like method [*Takeo et al.*, 2013]: We obtained 100 models from 100 combinations of dispersion curves ($c_m^1(\omega), c_m^2(\omega), \cdots, c_m^{100}(\omega)$) and defined one standard deviation as the model uncertainty. The obtained model is well constrained compared to the search range of 4–5 km/s in the mantle and 1–4 km/s in the crust. The model uncertainty is ~0.5% at almost all depths in the mantle except for the value of ~1% at a depth shallower than 20 km. The model uncertainties for the three crustal layers are also large of 1%–2% due to limited

period range of surface wave analysis. The value of V_{SV} is larger than 4.5 km/s at depths shallower than 50 km, whereas it decreases at a depth range of 50–80 km.

4. Phase Velocity Anomalies and 1-D Azimuthally Anisotropic Model

V_{SV} model described in the previous section is based on the azimuthally and spatially averaged phase velocities of Rayleigh waves. In this section, we first show the azimuthal dependence of the phase velocities of the fundamental mode Rayleigh waves obtained from the ambient noise and from the teleseismic surface waves. We then estimated one-dimensional azimuthally anisotropic model beneath the area of array.

4.1. Ambient Noise Cross-Correlation Analysis

The estimation of azimuthal anisotropy from ambient noise requires the measurements of phase velocity anomalies for all pairs of stations, which give phase velocity anomalies for various azimuths of surface wave propagations. We measured phase velocity anomalies and amplitude anomalies of 0*S* modes at periods of 10–30 s by fitting the synthetic CCF to the observed CCF for each pair of stations at each frequency band. The frequency range is from $0.9f_0$ to $1.1f_0$, where f_0 is the mean frequency. The synthetic cross spectra for a pair of *i*th and *j*th stations is

$$S''^{kl}_{ij} = (1+\zeta^{kl}_{ij})a^{kl}_{0S}J_0\left(\frac{\omega d_{ij}}{(1+\gamma^{kl}_{ij})c_{0S}}\right) + a^{kl}_{1S}J_0\left(\frac{\omega d_{ij}}{c_{1S}}\right), \tag{8}$$

where ζ^{kl}_{ij} and γ^{kl}_{ij} are the amplitude anomaly and phase velocity anomaly for the 0*S* mode, whereas a^{kl}_{nS} and c_{nS} are average amplitude and phase velocities of *n*th mode defined in equation (2). The synthetic and observed CCFs were obtained by applying band-pass filters to cross spectra in the frequency domain and by calculating inverse Fourier transforms. The optimal values of ζ^{kl}_{ij} and γ^{kl}_{ij} are then searched. Although we included the term of the 1*S* mode with average amplitudes and average phase velocities for measuring phase velocity anomaly of 0*S* mode, we could not measure the phase velocity anomalies of the 1*S* mode because of strong 2π ambiguity, i.e., two phase velocities with the difference of ~3% could fit the waveforms similarly because of short wavelength (~20–40 km) of the 1*S* mode compared to the interstation distances (~100–600 km).

We then examined the trade-off between inhomogeneous source distribution and the azimuthal anisotropy. The above analyses in this study are based on the theoretical cross spectrum with the assumption of homogeneous source distribution obtained by *Aki* [1957]. *Cox* [1973] derived the theoretical cross spectrum for the case of inhomogeneous source distribution explained by the Fourier series as

$$B(\phi) = B_0 + \sum_n B_n \cos\left[n(\phi-\phi_n)\right], \tag{9}$$

where ϕ is the back azimuth and B_n and ϕ_n denote intensity of and maximum azimuth of source heterogeneity for the *n*th term. The theoretical cross spectrum for the vertical component is then given by

$$S(\phi) = B_0 J_0\left(\frac{\omega d}{c}\right) + 2\sum_n i^n B_n \cos\left[n(\phi-\phi_n)\right] J_n\left(\frac{\omega d}{c}\right), \tag{10}$$

where ϕ is the azimuth of the great circle between the pair of stations d and c are interstation distance and phase velocity of a mode, respectively. The symbol i here remarks the imaginary unit. Since the odd order components of inhomogeneous source distribution $(B_1, B_3, B_5, \cdots)$ only causes imaginary term, we can avoid the effects of odd order components by only using real components of obtained cross spectra. We then evaluated the effects of even order components of inhomogeneous source distribution $(B_2, B_4, B_6, \cdots)$.

Weaver et al. [2009] estimated the effects of inhomogeneous source distribution to the phase velocity measurement. They calculated the change in the zero-crossing frequency, and the change in traveltime anomaly caused by the second term in equation (10). The apparent phase velocity anomaly is

$$\gamma_s = \frac{1}{2\omega^2\tau^2}\frac{B''(\phi)}{B(\phi)} = \frac{1}{8\pi^2}\left(\frac{\lambda'}{d}\right)^2\frac{B''(\phi)}{B(\phi)} \sim \frac{1}{8\pi^2}\left(\frac{\lambda'}{d}\right)^2\sum_n n^2\frac{B_n}{B_0}\cos\left[n(\phi-\phi_n)\right], \tag{11}$$

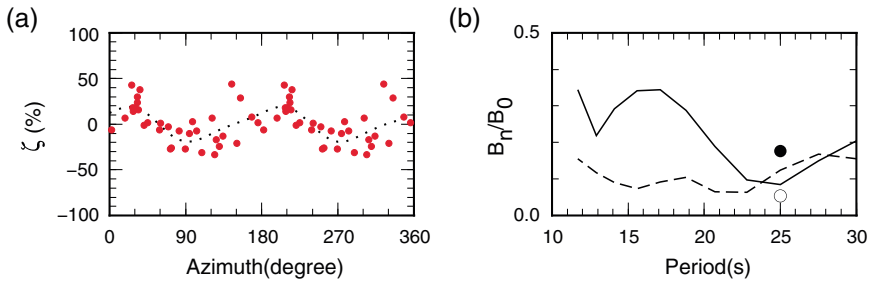

Figure 4. (a) Amplitude anomalies of 0*S* mode in CCFs, ζ_{ij}^{kl}, at a period of 21 s as a function of azimuth between two stations. The dotted curve is the fitting curve. (b) The intensity of even order components of source heterogeneity represented by B_2/B_0 (solid line) and B_4/B_0 (dashed line). Circles show the values of B_2/B_0 (filled) and B_4/B_0 (open) at a period of 25 s in the south California region estimated by *Harmon et al.* [2010].

where τ is the travel time, $\lambda' = u/f$ is almost equivalent to the wavelength $\lambda = c/f$, f is frequency, and u is the group velocity. This anomaly cannot be neglected when the interstation distance is comparable or shorter than the wavelength or when the source distribution is highly inhomogeneous.

Figures 4a shows the obtained amplitude anomalies, ζ_{ij}^{kl}, as a function of station-to-station azimuth. The fitting curves are obtained by considering B_0, B_2, and B_4 terms in equation (9), i.e., $B = B_0 + B_2 \cos 2(\phi - \phi_2) + B_4 \cos 4(\phi - \phi_4)$. Figure 4b shows the intensity of source heterogeneity represented by B_2/B_0 and B_4/B_0. The values are $B_2/B_0 = 0.1-0.3$ and $B_4/B_0 = 0.1-0.2$ for the 0*S* mode at periods of 10–30 s. *Harmon et al.* [2010] obtained similar intensity of source heterogeneity in the south California region at a period of 25 s. The maximum effects of source heterogeneity to the phase velocity anomalies are then $\gamma_s \sim (\lambda'/d)^2 \times 5\%$ from equation (11). The typical value of γ_s is smaller than 1% because the interstation distances (>100–200 km) are longer than the twice of the wavelength at periods shorter than ~25 s.

Figure 5a shows the phase velocity anomalies, γ_{ij}^{kl}, after the correction of water depth effect, γ_w, and inhomogeneous source distribution effect, γ_s, as a function of station-to-station azimuth. The values with the error larger than 2% were discarded, where the errors of phase velocity anomalies were estimated by considering signal-to-noise ratio of each CCF [*Takeo et al.*, 2014]. The variation in water depth affects the phase velocity anomalies, e.g., more than 1% in previous study [*Takeo et al.*, 2014]. The estimated effect in this study is smaller than 1% at periods longer than 15 s, which was corrected but not shown because of the small value. The azimuthal dependence seems to be dominated by cos 2ϕ term and is consistent with the theoretical prediction that the Rayleigh waves mainly have cos 2ϕ term by reflecting the cos 2ϕ azimuthal anisotropy of V_{SV} [e.g., *Montagner and Nataf*, 1986]. Figure 5a also shows the fitting line by

$$\gamma = A_2 \cos 2(\phi - \phi_{\max}), \tag{12}$$

where A_2 means the half intensity of azimuthal anisotropy and $\phi_{\max}$ means the fastest azimuth, the azimuth of maximum velocity. The errors of A_2 and $\phi_{\max}$ were obtained by the bootstrap method [*Efron*, 1979]. Figure 5c summarizes the peak-to-peak intensity ($2A_2$) and the fastest direction ($\phi_{\max}$) as a function of period. The fitting by cos 2ϕ term in Figure 5a is not perfect because lateral heterogeneity exists both in the isotropic and azimuthally anisotropic structures in this area as discussed in section 6.2. We here consider that the fitting by 2ϕ term is appropriate because the peak-to-peak intensity of cos 2ϕ term is significantly larger than 0 even if we consider the uncertainty (Figure 5c).

4.2. Teleseismic Event Array Analysis

Figure 5b shows the azimuthal dependence of phase velocities of the 0*S* mode for the case of teleseismic events. They are dominated by cos 2ϕ term similarly to the case of ambient noise analysis (Figure 5a). We estimated the frequency dependence of azimuthal anisotropy that maximizes the cross-correlation coefficients defined in equation (5). The azimuthal dependence can be represented by

$$c(\omega) = c_0(\omega)\,[1 + a\cos(2\phi) + b\sin(2\phi)]\,, \tag{13}$$

where $c_0(\omega) = \sum_n p'_n g^n(\omega)$, $a(\omega) = \sum_n a'_n g^n(\omega)$, and $b(\omega) = \sum_n b'_n g^n(\omega)$. The half intensity and the fastest direction of azimuthal anisotropy are then given by $A_2 = \sqrt{a^2 + b^2}$ and $\phi_{\max} = \tan^{-1}(b/a)$, respectively.

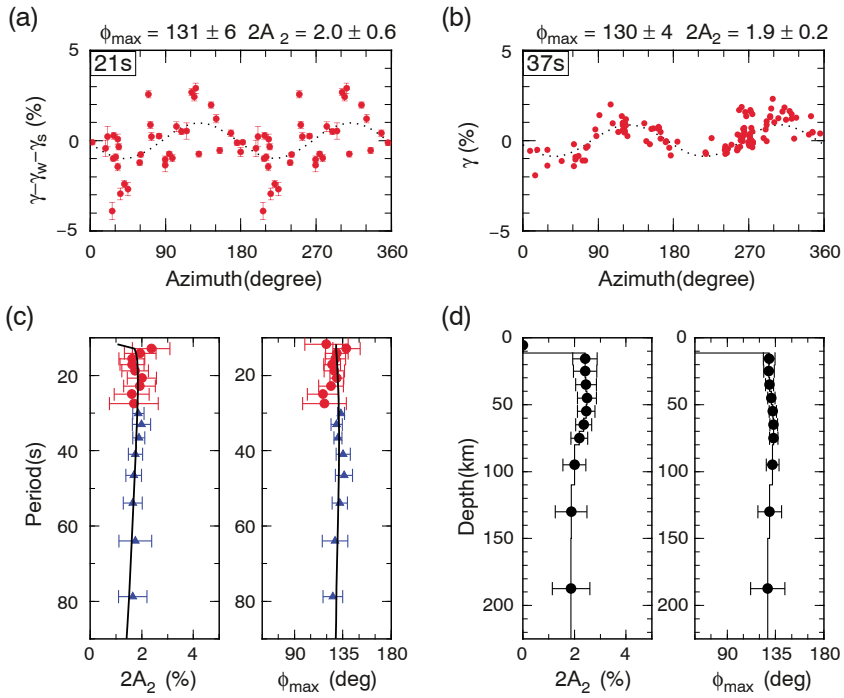

Figure 5. (a) Phase velocity anomalies of 0*S* mode at periods of 21 s obtained from ambient noise after the correction of effects from water depth and source heterogeneity, $\gamma_{ij}^{kl} - \gamma_w - \gamma_s$, as a function of propagation azimuths. The dotted curve is the fitting curve by cos 2ϕ pattern. (b) Same as Figure 5a but for a period of 37 s obtained from teleseismic waves. (c) The peak-to-peak intensity ($2A_2$) and the fastest direction (ϕ_{max}) estimated from ambient noise (red circles) and teleseismic surface waves (blue triangles) as a function of period. The solid line shows the theoretical values of the models shown in Figure 5d. (d) The model for the azimuthal anisotropy of V_{SV} corresponding to the smoothing parameter of ϵ_{AA} = 0.1. The model deeper than 100 km is not well resolved as shown by synthetic test (Figure 10).

Figure 5c summarizes the obtained values as well as those obtained from the ambient noise. The measurement errors for the teleseismic analysis are small compared to those from the ambient noise. For the case of teleseismic analysis, the lateral heterogeneity within the area of array can be averaged out by using all the stations simultaneously for each event. For the case of ambient noise analysis, on the other hand, the heterogeneity is averaged only over the path between each pair of stations. The lateral heterogeneity, thus, affects the phase velocity anomaly between each station pair and provides larger variation between measurements compared to the teleseismic analysis.

4.3. 1-D Azimuthally Anisotropic Model

The phase velocities of Rayleigh waves are mainly sensitive to V_{SV}. Although the azimuthal dependence of V_{SV} mainly have cos 2ϕ and cos 4ϕ components [e.g., *Crampin*, 1982], the cos 4ϕ term have small effect to the azimuthal dependence of the phase velocities of Rayleigh waves [e.g., *Montagner and Nataf*, 1986]. Based on this theoretical prediction and the clear domination of cos 2ϕ term (Figure 5), we here assume that the 2ϕ term azimuthal anisotropy of Rayleigh waves reflects that of V_{SV} and estimates the azimuthal anisotropy of V_{SV}.

We describe the azimuthal dependence of V_{SV} by $V_{SV}^0(z)(1 + A_C'(z)\cos 2\phi + A_S'(z)\sin 2\phi)$, as a function of depth (z), and estimate $A_C'(z)$ and $A_S'(z)$ in each of 10 layers in the uppermost mantle at depths of 12–225 km by assuming a constant value for each layer. The crust is assumed to be isotropic based on weak anisotropy compared to that in the mantle reported by previous studies [e.g., *Christensen and Salisbury*, 1975; *Dunn and Toomey*, 2001]. The model azimuthal anisotropy of Rayleigh waves is then given by

$$c(\omega) = c^0(\omega)\left[1 + \tilde{A}_C(\omega)\cos 2\phi + \tilde{A}_S(\omega)\sin 2\phi\right], \tag{14}$$

where

$$\tilde{A}_C(\omega) = \int_z \left[K_\beta(z,\omega)\right] A_C'(z)\, dz, \tag{15}$$

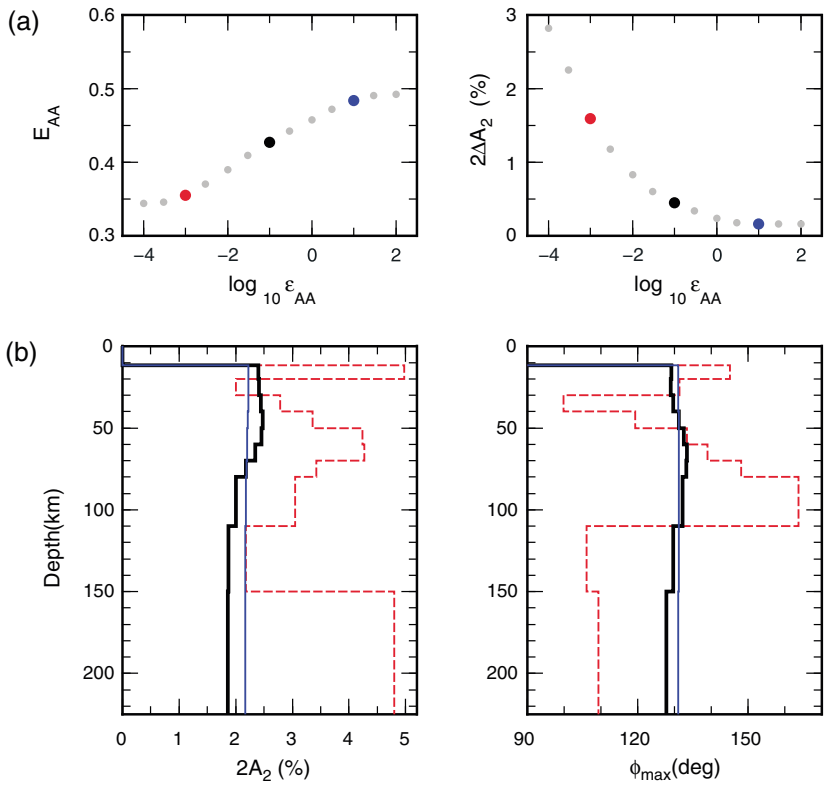

Figure 6. (a) Misfit, E_{AA}, and model variance for the peak-to-peak intensity of azimuthal anisotropy averaged for all 10 layers, $2\Delta A_2$, as a function of smoothing parameter, ϵ_{AA}. (b) Obtained azimuthally anisotropic models for three smoothing parameters ($\epsilon_{AA} = 0.001, 0.1, 10$). The color corresponds to each smoothing parameter plotted in Figure 6a. The model for $\epsilon_{AA} = 0.1$ (thick black line) is equivalent to the model shown in Figure 5d.

$$\tilde{A}_S(\omega) = \int_z \left[K_\beta(z,\omega)\right] A'_S(z)\, dz, \tag{16}$$

and K_β is the sensitivity of phase velocity to V_{SV}. The sensitivity kernel is obtained from the smooth 1-D V_{SV} model (Figure 3b). The use of sensitivity kernels for the azimuthally isotropic model is valid if the second-order perturbation can be neglected, i.e., the intensity of azimuthal anisotropy is less than ~10%.

We here define the misfit function by

$$E'_{AA} = E_{AA} + \epsilon_{AA} R_{AA} \tag{17}$$

$$= \frac{1}{2N_m} \sum_\omega \left[\left\{ \frac{\bar{A}_C(\omega) - \tilde{A}_C(\omega)}{\Delta A_C(\omega)} \right\}^2 + \left\{ \frac{\bar{A}_S(\omega) - \tilde{A}_S(\omega)}{\Delta A_S(\omega)} \right\}^2 \right] \tag{18}$$

$$+ \epsilon_{AA} \sum_{i=1}^{N-1} \left[\left(A''^{i+1}_C - A''^{i}_C \right)^2 + \left(A''^{i+1}_S - A''^{i}_S \right)^2 \right], \tag{19}$$

where N_m is the number of measurements, $\bar{A}_C(\omega)$ and $\bar{A}_S(\omega)$ are the bootstrap averages of the estimated azimuthal anisotropy of phase velocities, and $\Delta A_C(\omega)$ and $\Delta A_S(\omega)$ are errors on the measurements. The smoothing term is again introduced as the second term to reduce the uncertainty related to the trade-off between adjacent layers, where ϵ_{AA} is a constant smoothing parameter, A''^{i}_C and A''^{i}_S are A'_C and A'_S in the ith layer and $N = 10$ is the number of layers. We here used the fast simulated annealing algorithm [*Szu and Hartley*, 1987; *Nam et al.*, 2004] to deal with larger number of model parameters, 20, compared to that for isotropic inversion, 13. The model uncertainty was estimated from 100 samples (A^l_C and A^l_S; $l = 1, \cdots, 100$) obtained by the bootstrap method.

Figure 5c shows the fitting between the measured and model intensities of surface wave azimuthal anisotropy. Figure 5d shows the obtained one-dimensional azimuthally anisotropic structure including the intensity and

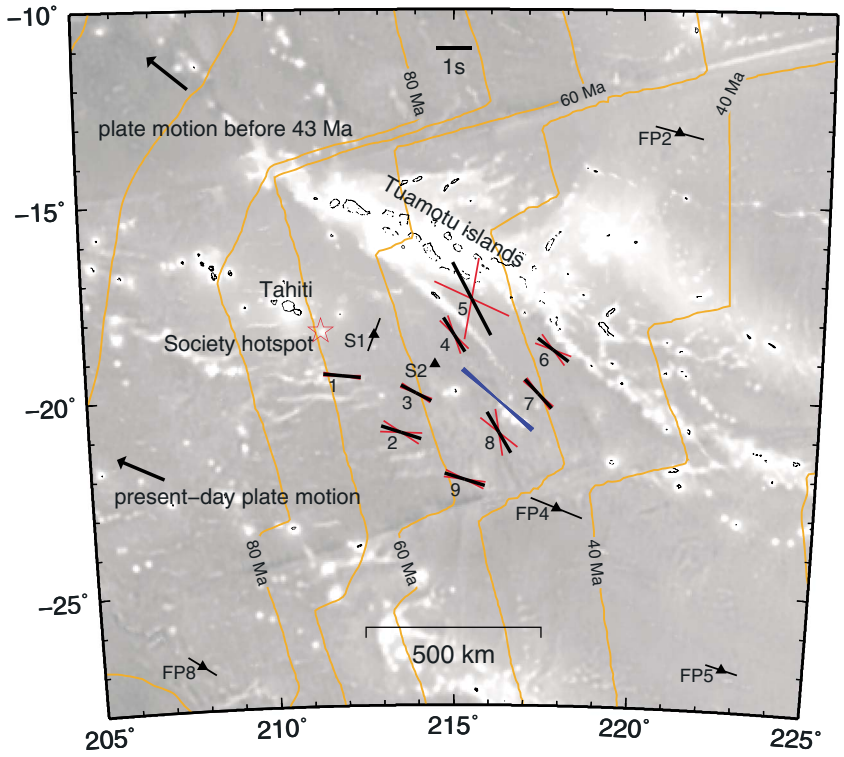

Figure 7. The azimuth of maximum *S* wave velocity in six layers at depths of 20–80 km estimated from surface waves (blue bars) and beneath each station estimated from shear wave splittings in this study (thick black bars with the red bars showing the uncertainty; labeled 1–9 to reflect station names of SOC1–SOC9) and by *Barruol et al.* [2009] in the area of this map (thin black bars with triangles labeled S1, S2, FP2, FP4, FP5, and FP8). The lengths of black bars for the splitting analysis show the splitting time, whereas the length of blue bars for the surface wave is arbitrary chosen. Orange lines show the seafloor isochrones [*Müller et al.*, 2008] with the contour interval of 10 Ma.

the azimuth of maximum V_{SV}. In general, the misfit E_{AA} is smaller and the model variance is larger for a smaller smoothing parameter (an example for the case of radially anisotropic inversion by *Takeo et al.* [2013]). Figure 6 shows the misfit, model variance, and obtained azimuthally anisotropic models for various smoothing parameters. The models are almost constant with depth for $\epsilon_{AA} \geq 0.1$ because of the small period dependence of azimuthal anisotropy of Rayleigh waves in this study (Figure 5c). Although the structure starts to fluctuate and the misfit decreases for smaller smoothing parameters, the fluctuation is not significant compared to the increasing model variance. We therefore chose the smoothing parameter of $\epsilon_{AA} = 0.1$. The choice of $\epsilon_{AA} = 0.1$ is also valid because the corresponding model variance is almost equivalent to the uncertainty of measured azimuthal anisotropy (Figure 5c). The model uncertainty for the peak-to-peak intensity ($2A_2$) is then 0.5% (Figure 5d). The obtained peak-to-peak intensity is 2%–3%. The fastest azimuth is NW–SE direction as shown by blue bars in Figure 7.

5. Shear Wave Splitting Analysis

Previous studies suggested the presence of lateral variation of the azimuthal anisotropy in a broader area including the area in this study by the shear wave splitting analysis of island records [*Fontaine et al.*, 2007] and seafloor records [*Barruol et al.*, 2009]. To reveal the lateral variation within the array, we applied a method of shear wave splitting analysis by *Silver and Chan* [1991] to the records of nine BBOBSs.

The events were first chosen with two criterions: (i) the moment magnitude greater than 5.5 and (ii) the epicentral distance larger than 9000 km or the hypocenter depth deeper than 200 km. The events with epicentral distances larger than 9000 km show the arrival of SKS and/or SKKS wave, whose splitting mainly reflect the azimuthal anisotropy beneath the station integrated from the core-mantle boundary to the surface. The events with shorter epicentral distances show the arrival of direct *S* wave, whose splitting reflects the azimuthal anisotropy along whole ray path. For the epicentral distance shorter than 9000 km, therefore,

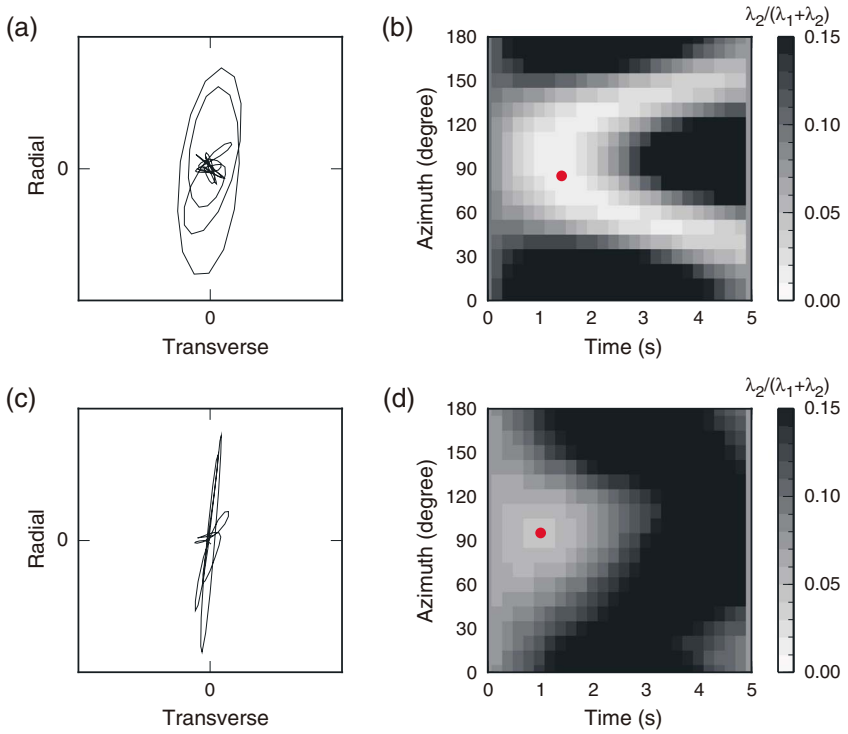

Figure 8. (a) An example of horizontal particle motion of SKKS wave at station SOC1 for an event occurred at 1:13, 18 February 2010 (UT). The epicentral distance is 143°. (b) The ratio, $\lambda_{ratio} = \lambda_2/(\lambda_1 + \lambda_2)$, defined by smaller and larger eigen values, λ_1 and λ_2, as a function of assumed lag time and assumed azimuth of maximum *S* wave velocity. Red circle shows the minimum of the ratio. (c) Particle motion after the correction of shear wave splitting for the value shown by red circle in Figure 8b. (d) The ratio averaged for all events at station SOC1.

the event with a depth shallower than 200 km should not be used to avoid the effect of near-source strong anisotropy at depths shallower than 200 km [e.g., *Long and van der Hilst*, 2005].

The waveforms of horizontal components were then band pass filtered with a period range of 10–20 s and were discarded if the signal-to-noise ratio is lower than 2. The signal amplitude is the root-mean-square amplitude of a 60 s long record centered at the peak of arrived signal. The noise amplitude is that of a 60 s long record prior to the time window for the signal amplitude. The band-pass filter is chosen to analyze the period range corresponding to minimum noise levels for BBOBSs (see example of noise level of BBOBS in *Suetsugu and Shiobara* [2014]). Figure 8a shows an example of particle motion for a SKKS waveform, which is elliptical due to splitting.

Silver and Chan [1991] proposed various strategies to search for the optimal splitting parameters, the splitting time (δt) and the azimuth of maximum *S* wave velocity (ϕ_{max}) that give the linear particle motion after the correction of splitting. We used the ratio between the smaller eigen value and the summation of eigen values, $\lambda_{ratio} = \lambda_2/(\lambda_1 + \lambda_2)$, to search the optimal splitting parameters. By choosing an optimal combination of parameters, the linear particle motion before the splitting can be reconstructed as shown by an example in Figure 8c.

The uncertainty of splitting parameters is usually large as indicated by the broad distribution of small λ_{ratio} shown in Figure 8b. We reduced the uncertainty by averaging λ_{ratio} of all events for each station as done by *Wolfe and Silver* [1998]. Figure 8d shows examples of the averaged values. The distribution of small λ_{ratio} is narrow and has less trade-off between two splitting parameters compared to the distribution for an event in Figure 8b. In addition, we could estimate the uncertainty of splitting parameters by the bootstrap method [*Efron*, 1979]: We estimated one hundred sets of parameters by selecting 100 combinations of events randomly with allowing overlaps and defined the one standard deviation as the uncertainty.

Figure 7 shows the estimated splitting parameters for each station as well as results from surface wave analysis. The number of available events was 8–14, in which more than half events showed splitting as summarized

Table 1. Station Location, Splitting Parameters, and the Numbers of Events

Station	Latitude	Longitude	Depth (m)	ϕ_{max} (deg)	δt (s)	N_{split}	$N_{unsplit}$
SOC1	−19.47°	−148.05°	4398	96 ± 5	1.0 ± 0.2	4	4
SOC2	−20.96°	−146.44°	4766	108 ± 16	1.1 ± 0.4	5	3
SOC3	−19.93°	−146.02°	4632	118 ± 7	0.9 ± 0.3	7	5
SOC4	−18.42°	−144.99°	4457	148 ± 14	1.1 ± 0.7	8	4
SOC5	−17.50°	−144.51°	4031	152 ± 38	2.3 ± 1.8	7	4
SOC6	−18.81°	−142.29°	4483	127 ± 17	1.1 ± 0.9	5	6
SOC7	−19.94°	−142.69°	4467	137 ± 7	1.1 ± 0.3	9	5
SOC8	−20.95°	−143.76°	4779	150 ± 21	1.3 ± 0.6	9	2
SOC9	−22.17°	−144.70°	4513	107 ± 10	1.2 ± 0.2	9	3

in Table 1. The events without splitting could be also used to constrain the fastest azimuths by the averaging method [*Wolfe and Silver*, 1998] because the absence of splitting under the presence of anisotropy means that the particle motion is parallel to the fastest or slowest azimuth. The splitting time is 1.0–1.3 s for almost all stations except for the station SOC5, which gives 2.3 ± 1.8 s. The uncertainty of the azimuth is also large for station SOC5, 152° ± 38°. For other stations, the uncertainty for the splitting time is 0.2–0.9 s, and the uncertainty of the azimuth is less than 22°. The azimuth is almost parallel to each other, although it is slightly northward for the northeastern stations (SOC4–SOC8) and is slightly westward for the northwestern station (SOC1).

6. Discussions

We here first discuss the depth of lithosphere-asthenosphere boundary based on isotropic V_{SV} model in Figure 3b. We then discuss lateral heterogeneity, depth dependence, and intensity of azimuthal anisotropy based on azimuthally anisotropic model in Figure 5d and the result of shear wave splitting analysis in Figure 7. The difficulty of estimating radial anisotropy will be mentioned shortly at the end.

6.1. Depth of Lithosphere-Asthenosphere Boundary

The depth of lithosphere-asthenosphere boundary (LAB) needs to be clarified for discussing whether a certain depth is corresponding to the lithosphere or the asthenosphere. In general, the sharp boundary between the lid and LVZ cannot be retrieved from surface waves due to long vertical wave lengths of surface waves. Previous surface wave tomography studies have, therefore, defined the maximum velocity gradient as the LAB [e.g., *Burgos et al.*, 2014; *Yoshizawa and Kennett*, 2015]. Our isotropic V_{SV} model (Figure 3) shows constant velocity within the uncertainty range at a depth range of 10–40 km, large velocity reduction at a depth range of 40–80 km, and almost constant velocity at a depth range of 80–150 km. The deeper depth is constrained by the velocity at a depth range of 110–150 km and the velocity of the ORM model at a depth of 225 km. Although the velocity reduction at a depth range of ~40–80 km is gradual, the sharpness might be affected by the vertical smoothing during the structural inversion [*Takeo et al.*, 2013], i.e., the actual structure beneath our study area may have sharp velocity reduction at a depth of 60 km. The depth of velocity reduction can be more clearly estimated by measuring phase velocities of the fundamental mode Love wave, which has sensitivity to shear wave velocity structure in the lid but could not be measured in this study due to effect of the higher modes of Love wave (section 6.5). We hereafter simply interpret that the LAB exists at a depth of 60 km beneath the area of this study.

The depth of LAB has been estimated in various oceanic regions using body and surface waves. We obtained the depth of 60 km for the average seafloor age of 60 Ma in the French Polynesia region located inside the area of the South Pacific superswell. According to previous studies, LAB depth at the seafloor age is estimated to be 60–80 km from body waves [*Kumar and Kawakatsu*, 2011] and 80–100 km from vertical velocity gradient of surface wave tomography models [*Burgos et al.*, 2014]. Although our estimation has a large uncertainty of ~20 km, our value is at the shallowest value in the range by previous studies possibly due to reheating and thinning of the lithosphere caused by the hot plumes beneath the South Pacific superswell [*Adam and Bonneville*, 2005]. The shallower LAB in the South Pacific superswell region compared to other regions of the similar seafloor ages can be also recognized in results of surface wave tomography [*Burgos et al.*, 2014] and body wave studies [*Rychert and Shearer*, 2011; *Schmerr*, 2012].

6.2. Lateral Heterogeneity

The presence of crustal lateral heterogeneity should be discussed because the seafloor topography is highly heterogeneous and the crustal thickness is thicker when the topography is high [e.g., *Patriat et al.*, 2002]. The effect to the azimuthal anisotropy measurement is fortunately small in this study because the 0*S* mode used in this study has little sensitivity to *S* wave velocity at depths shallower than ~20 km (see *Takeo et al.* [2013] for an example of the depth dependence of sensitivity).

The lateral heterogeneity of azimuthal anisotropy should be also discussed. *Fontaine et al.* [2007] applied shear wave splitting analysis to records of island stations in the French Polynesia region around the area in this study. *Barruol et al.* [2009] further analyzed shear wave splitting by using BBOBS records of previous Japan-France cooperative project [*Suetsugu et al.*, 2005]. They showed that the fastest azimuth is almost consistent with the current plate motion except for the region southeast of the Tahiti island where the azimuth is almost perpendicular to the plate motion (S1 in Figure 7) or no anisotropy (S2 in Figure 7), although they determined the fastest azimuth or the absence of azimuthal anisotropy from one or zero splitting event out of 8–13 events analyzed in total. We estimated the azimuthal anisotropy by analyzing the shear wave splitting from records of more densely deployed BBOBSs. Since 4–9 events showed splitting of *S*, SKS, or SKKS waves for each station (Table 1), we conclude that there is azimuthal anisotropy within the area of this study with the fastest azimuth roughly parallel to the current plate motion.

We then compared the fastest azimuths estimated from surface waves and shear wave splittings in this and previous studies. The fastest azimuths obtained in this study are 96°–118° for southwestern stations (SOC1–SOC3 and SOC9) and 127°–152° for northeastern stations (SOC4–SOC8). The values for the southwestern stations are similar to the values of previous results in wider area [*Fontaine et al.*, 2007; *Barruol et al.*, 2009], whereas the northeastern stations have different fastest azimuths. This difference suggests that the northeastern part is more perturbed by local phenomena, such as the ancient activity formed the Tuamotu plateau [*Ito et al.*, 1995], compared to the southwestern part of the area in this study.

On the other hand, we obtained average azimuthal anisotropy within the area with the fastest azimuth of 130° ± 5° from teleseismic surface waves, which is between the values obtained from shear wave splittings in this study. This can be understood by considering two areas with different fastest azimuths: ϕ_{max}=110° and ϕ_{max} = 140°. The azimuthal dependences of surface wave phase velocities are then cos2(ϕ-110°) and cos 2 (ϕ − 140°) for two areas and cos (140°-110°) cos 2[ϕ-(110°+140°)/2)] = 0.87 cos 2(ϕ-125°) for the average. These equations show that the surface wave analysis gives the average of fastest azimuths with a small reduction in the intensity of up to 13% if the variation in the azimuths is less than 30°.

The fastest azimuth for the station SOC1 is largely different from the average for all other stations compared to the small uncertainty of fastest azimuth. If we discard the result for station SOC1 and consider the uncertainty for the estimation, all the fastest azimuths for other stations of SOC2–SOC9 fall within the range between 117° and 134°, whereas the value for the station SOC1 is 96° ± 5° (Table 1). It indicates that the fastest azimuth estimated by surface waves may be affected by strong lateral variation in the fastest azimuths near station SOC1 (Figure 7). We therefore reestimated the azimuthal anisotropy of surface waves by discarding the records of SOC1. Figures 9a–9c show the azimuthal anisotropy of phase velocities of Rayleigh waves without station SOC1. We can now clearly find cos 2ϕ pattern in the azimuthal dependence of phase velocity anomalies measured not only from teleseismic surface waves (Figure 9b) but also from ambient noise (Figure 9a). The pattern was not clear for the phase velocity anomalies measured from ambient noise using all the stations (Figure 5a). Figure 9d is the corresponding one-dimensional model of azimuthal anisotropy. The intensity of azimuthal anisotropy is ~30% larger for the model without station SOC1 than the model for all stations at depths shallower than 60 km. The change in the fastest azimuth is less than 10° and negligible. The reduction of the intensity by including SOC1 also suggests that lateral heterogeneity of the fastest azimuths exists at depths shallower than 60 km in the lithosphere.

6.3. Fastest Azimuths

The depth dependence of fastest azimuth has been discussed by previous studies. In general, the fastest azimuth is perpendicular to magnetic lineation in the lithosphere [e.g., *Francis*, 1969], whereas it is parallel to the current plate motion in the asthenosphere [e.g., *Tanimoto and Anderson*, 1984]. These interpretations are widely accepted and used to explain depth variations of fastest azimuths determined by recent tomography studies [*Smith et al.*, 2004; *Maggi et al.*, 2006b; *Debayle and Ricard*, 2013; *Burgos et al.*, 2014] (see also recent comparison by *Becker et al.* [2014]).

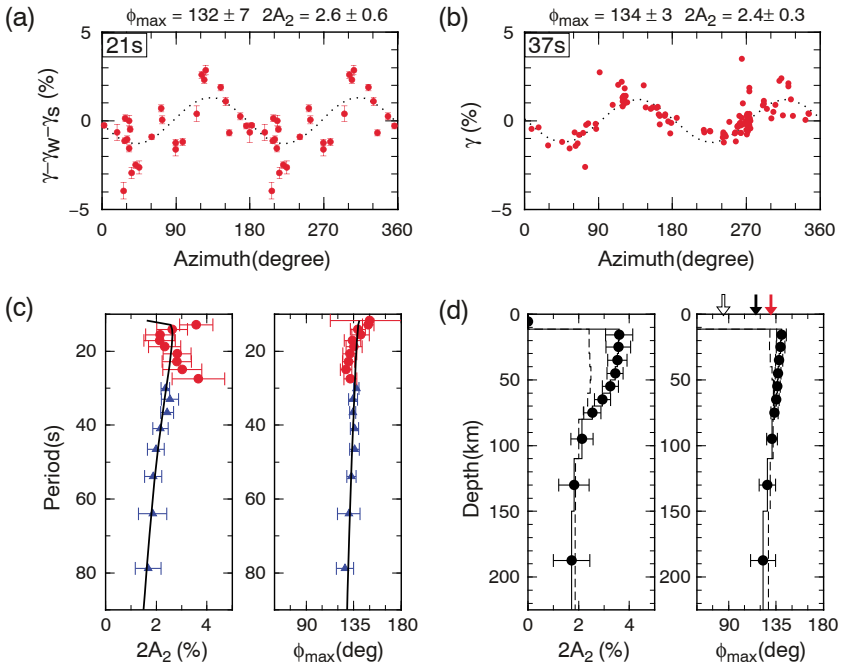

Figure 9. (a–d) Same as Figure 5, but except for station SOC1. (d) Dashed lines correspond to the model obtained by using all nine stations shown in Figure 5d. Three arrows at the top shows the direction perpendicular to magnetic lineations (open black), the direction of current plate motion (filled black), and the direction of ancient plate motion before 43 Ma (red).

We first examined the depth resolution of our azimuthally anisotropic model by synthetic tests. For given initial models, we calculated the theoretical values of measurements, the frequency dependence of the azimuthal anisotropy of phase velocities ($A_C(\omega)$ and $A_S(\omega)$). We then applied the same inversion code (section 4.3) to obtain structure for each initial model. The smoothing parameter is $\epsilon_{AA} = 0.1$, as same as the value used for inversions in this study. The measurement error obtained from the real data sets (Figure 9c) is added to the theoretical values to estimate the uncertainty of obtained models. Figure 10 shows the initial and obtained models. For the initial models, we chose the fastest azimuths almost perpendicular to magnetic lineation of our study area at shallow depths and the fastest azimuths almost parallel to current plate motion at deeper depths as discussed by previous studies [e.g., *Smith et al.*, 2004]. The obtained models show that the depth change in the fastest azimuth can be retrieved for the depth of 30 km or 80 km (Figures 10b and 10c), whereas the change in fastest azimuth cannot be retrieved for a depth of 20 km (Figure 10a) or a depth of 110 km (Figure 10d). The intensity of anisotropy can be roughly retrieved except for the depth where the change in the fastest azimuth is sharp. These results indicate that our azimuthally anisotropic model (Figure 9) is well constrained at depths of ~20–100 km, from middle and lower parts of lithosphere at depths of 20–60 km to the top of the asthenosphere at depths of 60–100 km. We have less resolution at depths shallower than 20 km due to lack of phase velocity anomaly for the 1*S* mode at periods shorter than 20 s, which could be analyzed in previous OBS analysis [*Takeo et al.*, 2014] but not in this study because of longer interstation distances. We also have less resolution at depths deeper than 100 km due to lack of analysis for the 0*S* mode at periods longer than 100 s.

We then interpret the fastest azimuth at depths of 20–50 km in the middle lithosphere. In general, there is no current deformation in this depth range, but there was deformation when the seafloor was younger. Previous studies have, thus, considered that anisotropy in the lithosphere preserves ancient mantle flow perpendicular to the ancient spreading axis, whose direction is recorded as the direction of magnetic lineations [e.g., *Nishimura and Forsyth*, 1989]. Our result, however, shows that the fastest azimuth is NE–SE direction (135–140°) and is not perpendicular to the magnetic lineation of NNW-SSE (85°; Figures 7 and 9). The resolution test (Figure 10b) indicates that we can detect the depth change of fastest azimuths if the change exists between depths of 20 and 100 km. The absence of the change of direction in our result (Figure 9) means that the fastest azimuths is NE–SE at least at a depth range of 20–100 km. For understanding when this depth

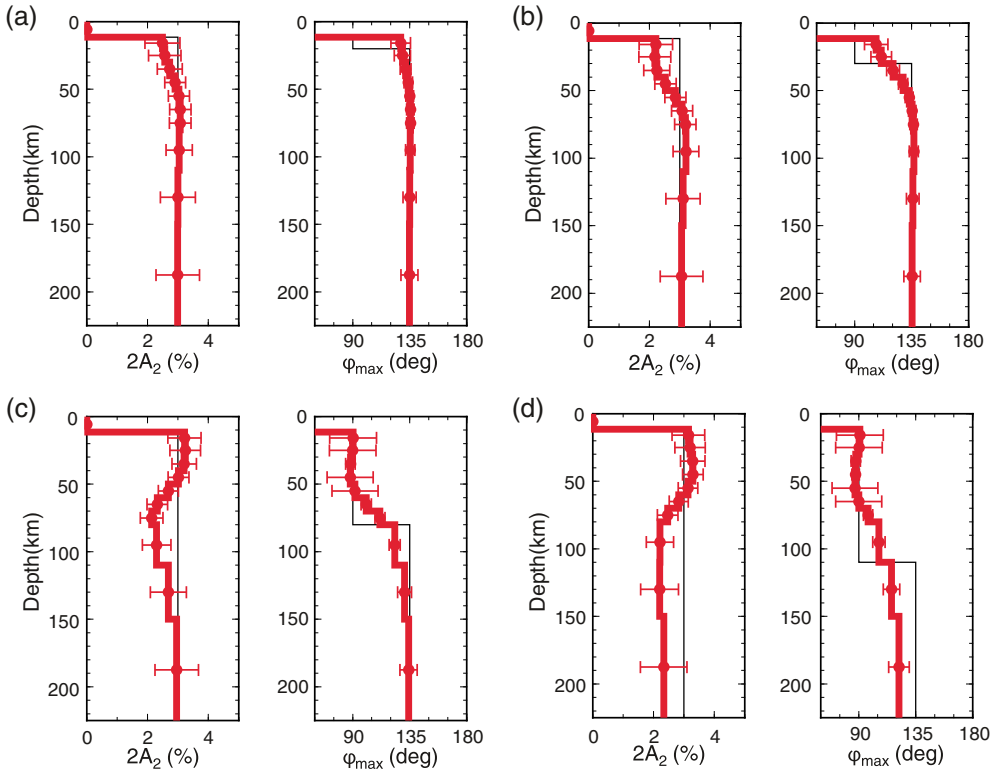

Figure 10. The initial (thin black) and retrieved (thick red) models of the synthetic test. The fastest azimuth of initial model is changed from 90 to 135° at depths of (a) 20 km, (b) 30 km, (c) 80 km, and (d) 110 km.

range experienced deformation, we here look at the depths of LAB in other oceanic regions. According to observations [e.g., *Kumar and Kawakatsu*, 2011] and models [e.g., *Karato*, 2012], the LAB is at a depth of ~50 km for the seafloor age of 10–20 Ma, i.e., the depths shallower than ~50 km become lithosphere within 10–20 Ma from the seafloor spreading. For the area of this study with a seafloor age of 60 Ma, the depths shallower than 50 km seem to have deformed 40–60 Ma ago. Our results, thus, mean that the ancient mantle flow at 40–60 Ma ago beneath this region was not perpendicular to the ancient mid-ocean ridge at least at a depth range of 20–50 km.

An interpretation emerges when we realize that the fastest azimuths are parallel to the plate motion before 43 Ma [*Schlanger et al.*, 1984; *Ito et al.*, 1995]. As compiled by *Seton et al.* [2012], the ancient plate motion before 43 Ma in this region was not perpendicular to the ancient mid-ocean ridge during the seafloor spreading of this region. Such complicated situation at the era was caused by the passive seafloor spreading in this region compared to an active seafloor spreading between the Pacific Plate and the Antarctica Plate at the southwest of this region. The fastest azimuth estimated in this study, therefore, implies that the mantle flow is not perpendicular to the magnetic lineation as stated by previous studies [e.g., *Francis*, 1969; *Smith et al.*, 2004] but can be parallel to the ancient plate motion when the ancient plate motion was not perpendicular to the ancient mid-ocean ridge. *Toomey et al.* [2007] reported similar results near ridge segmentation region from Pn wave anisotropy. They showed that the fastest azimuths were between the direction of plate motion and the direction perpendicular to the mid-ocean ridge at depths shallower than ~20 km. Our results suggest that the direction of plate motion affects seismic anisotropy at depths deeper than 20 km. The similar discussion has been implied from the results of previous surface wave tomography studies but could be clearly shown by this study because we have better resolution of azimuthal anisotropy compared to previous studies for the limited area. Our result also suggests the possibility of reconstructing ancient mantle flow from surface waves by deploying arrays of broadband OBSs in various oceanic regions.

The fastest azimuth at depths deeper than 50 km is estimated to be ~130°. The difference between the observed fastest azimuth and current plate motion, 116° (HS3-NUVEL-1) [*Gripp and Gordon*, 2002], suggests that the flow in the asthenosphere is perturbed by the presence of the Society hot spot as already discussed

and indicated from previous shear wave splitting analysis [*Barruol et al.*, 2009]. It should be noted that the difference can be also explained by vertical smoothing during the azimuthally anisotropic inversion (see Figure 10 for synthetic tests) because the obtained fastest azimuths at depths deeper than 100 km is ~120°, more closed to the azimuth of current plate motion compared to the fastest azimuth at depths shallower than 50 km of 135°. The model uncertainty is, however, too large at depth deeper than 100 km to discuss in detail. The fastest azimuths also varied with place inside the our study area at a depth shallower than 60 km in the lithosphere (section 6.2). Since there should be no or small current deformation in the lithosphere, the lateral variation suggests the effect of ancient hot spot activity at the Tuamotu plateau [*Ito et al.*, 1995] to the flow of mantle before ~40 Ma.

6.4. Intensity and Depth Extent of Azimuthal Anisotropy

The intensity of anisotropy is essential to discuss the deformation mechanism and shear strain in the mantle. In previous studies, the intensity of azimuthal anisotropy is estimated to be up to 10% at depths shallower than ~20 km by refraction surveys (see a compile by *Song and Kim* [2012]). At deeper depth, the intensity of azimuthal anisotropy has been mainly estimated to be ~2% by surface wave tomography studies [*Smith et al.*, 2004; *Maggi et al.*, 2006b; *Debayle and Ricard*, 2013; *Yuan and Beghein*, 2013; *Burgos et al.*, 2014], although the quantitative estimation of the intensity is difficult for the tomography studies [*Smith et al.*, 2004].

In this study, we could estimate the azimuthal anisotropy of V_{SV} at depths of 20–100 km in oceanic lithosphere/asthenosphere system for the first time from broadband array analysis of surface waves. The obtained intensity is less uncertain compared to previous tomography studies because we used more data sets within the area of interest and we estimated the intensity of azimuthal anisotropy without using lateral smoothing parameters, although we assumed homogeneous azimuthal anisotropy within the area. We first compare our results with previous studies at depths shallower than 50 km and deeper than 50 km independently and then discuss the depth change.

The obtained model for the relatively homogeneous area (Figure 9) shows the peak-to-peak intensity of 3%–4% at depths of 20–50 km. The value is slightly smaller than the intensity of Pn wave anisotropy in other oceanic regions determined by refraction surveys. The first reason is that the intensity of azimuthal anisotropy is ~30% stronger for the *P* wave than for *S* wave, which is expected from elastic constants of olivine crystals [*Kumazawa and Anderson*, 1969] and also observed by a refraction survey in the northwest Pacific Ocean [*Shinohara et al.*, 2008]. Another reason is that the half spreading rate of the seafloor in this study is 2–3 cm/yr [*Müller et al.*, 2008], relatively smaller than other oceanic regions. According to *Song and Kim* [2012], the intensity of Pn wave anisotropy linearly correlates with the spreading rate and is ~4% for the spreading rate of 2–3 cm/yr. The intensity of Sn wave anisotropy is then predicted to be ~3%. Our result is almost consistent with the predicted value if we consider the model uncertainty.

The intensity of anisotropy in the asthenosphere at depths of 50–100 km is 2%–3%. The value is roughly consistent with the intensity of azimuthal anisotropy in the asthenosphere determined by tomography studies [e.g., *Smith et al.*, 2004]. The consistency indicates that previous tomography studies have chosen reasonable smoothing parameter to constrain the intensity of azimuthal anisotropy in the asthenosphere. It should be noted recent tomography models [*Yuan and Beghein*, 2013; *Debayle and Ricard*, 2013] show local regions with the intensity stronger than 2%, which is not the case for the region of this study.

The depth change in the intensity of azimuthal anisotropy is dominant at a depth range of 50–80 km. As discussed above, this result is consistent with previous results of azimuthal anisotropy showing stronger anisotropy at the top of lithosphere from body waves and weaker anisotropy in the asthenosphere from surface waves. The stronger anisotropy indicates larger shear strain accumulated in the lithosphere when it formed near the mid-ocean ridge compared to the accumulated shear stain in the asthenosphere. These result and interpretation are, however, inconsistent with the stronger radial anisotropy in the asthenosphere shown by surface wave tomography studies [e.g., *Nettles and Dziewonski*, 2008] and larger strain accumulation in the asthenosphere expected from numerical simulations of mantle flow [e.g., *Behn et al.*, 2009]. This difference in the depth variations of azimuthal and radial anisotropy may be reflecting the different fabrics of the olivine crystals, which can change the ratio between the intensities of azimuthal and radial anisotropy [e.g., *Mainprice*, 2007]. We need to quantitatively compare the intensities of radial and azimuthal anisotropy in the future study to understand the shear accumulation and deformation mechanism in the mantle.

The depth extent of anisotropy is also a long existing question. An early study showed that radial anisotropy can be negligible at depths deeper than 300 km by analyzing multimode Love waves [*Cara and Lévêque*, 1988]. Recent surface wave tomography also shows that the azimuthal anisotropy is only significant in the top 200–250 km of the uppermost mantle [*Debayle and Ricard*, 2013] by analyzing higher modes of surface waves. On the other hand, previous studies have improved the depth resolution of azimuthal anisotropy by combining the results of shear wave splitting analysis and surface waves analysis [*Marone and Romanowicz*, 2007] based on the correlations between them [*Montagner et al.*, 2000; *Becker et al.*, 2012]. *Monteiller and Chevrot* [2011] estimated intensity of anisotropy in heterogeneous media by carefully considering the smoothing and damping effect to three-dimensional inversion based on shear wave splitting analysis.

Although our azimuthally anisotropic model only has enough resolution at a depth range of 20–100 km, we here roughly estimate the depth extent of azimuthal anisotropy in the asthenosphere by extrapolating our results at deeper and shallower depths and comparing the estimated splitting time with the observations. The original values for comparison are the azimuthally anisotropic model beneath stations SOC2–SOC9 determined at depths of 20–100 km from surface waves (Figure 9), and the observed splitting times of ~1.1 s (Table 1), which corresponds to the integral of azimuthal anisotropy in the mantle along the path of shear waves. Based on the relationship between the splitting time and azimuthally anisotropic model by surface waves [*Montagner et al.*, 2000], we can estimate the splitting time caused by anisotropy in the lid at depths of 10–60 km to be $\delta t_{\mathrm{lid}} = 0.35–0.43$ s. Although azimuthal anisotropy at depths of 10–20 km is not well resolved in this study, we here used the value of our model at the depth range of 10–20 km constrained smoothly by the depth range deeper than 20 km. If the fastest azimuths have the variation of 30° beneath stations SOC2–SOC9 as indicated from the splitting analysis (Figure 7), the azimuthal anisotropy is 13% underestimated. The splitting time due to anisotropy in the lid is then estimated to be $\delta t_{\mathrm{lid}} = 0.40–0.49$ s. By subtracting the value from the total splitting times of ~1.1 s, the splitting time due to anisotropy in the LVZ is estimated to be $\delta t_{\mathrm{LVZ}} = 0.6–0.7$ s.

The thickness of azimuthal layer in the LVZ is finally estimated to be $\delta t_{\mathrm{LVZ}}/(2A_2) \times 4.3$ km/s for a half intensity of azimuthal anisotropy in the LVZ of A_2. The thickness becomes 130–150 km for $A_2 = 1\%$, a reasonable value at a depth range of 60–100 km estimated in this study (Figure 9). If lateral variation of the fastest azimuths exists in the LVZ, the value of δt_{LVZ} becomes underestimated, i.e., the thickness becomes larger. If the fastest azimuths in the lid and LVZ are different, the thickness becomes underestimated because the total splitting time becomes less than the summation of δt_{lid} and δt_{LVZ} [*Montagner et al.*, 2000]. These possibilities of overestimation and underestimation due to vertical and lateral variations seem to cancel to each other. The splitting time, thus, indicates that the azimuthal anisotropy exists down to a depth of 190–210 km from the sea surface. This result is consistent with the maximum depth for the azimuthal anisotropy of 200–250 km suggested by previous surface wave study [*Debayle and Ricard*, 2013]. Since several tomography studies show strong radial anisotropy in the asthenosphere [*Nettles and Dziewonski*, 2008], the intensity of azimuthal anisotropy may be larger than the value assumed in the above discussion of 2%. The depth extent of azimuthal anisotropy then becomes shallower. We need to design larger array of BBOBSs to constrain intensity of azimuthal anisotropy at periods longer than 100 s to discuss the real depth extent of azimuthal anisotropy.

6.5. Difficulty of Estimating Radial Anisotropy

The estimation of radial anisotropy requires phase velocities of both Rayleigh and Love waves. In this study, we mainly analyzed Rayleigh waves to obtain V_{SV} structure and its azimuthal anisotropy. Although we attempted to analyze Love waves as previously done by *Takeo et al.* [2013] in the Shikoku Basin area, we could not use the phase velocities to estimate radial anisotropy in this study because the effect of first higher mode could not be evaluated at this moment. In previous study, for example, *Gaherty et al.* [1996] suggested the presence of significant overlapping of the higher mode to the fundamental mode of Love waves in oceanic regions. Since our isotropic V_{SV} model (Figure 3b) gives similar phase and group velocities for the two modes of Love waves, their significant overlapping seems to exist in our data sets. The two modes can be isolated if we can observe the swell of the amplitude due to interference between them. The expected wavelength of the swell is, however, of the order of 4000–8000 km at a period range of 10–50 s, which is hard to resolve with the current array size of 500 km. The raypath, or the array size, needs to be larger to resolve the interference between multimodes of Love waves as previously done for long paths by *Cara and Lévêque* [1988]. The higher modes might also affect the measured phase velocities of the fundamental mode Love wave for the Shikoku Basin by *Takeo et al.* [2013]. In the future study, we need to evaluate the effect of higher modes on the phase

velocity measurements of the fundamental mode of Love wave and obtain radially anisotropic models beneath oceanic regions, which is beyond the scope of this study.

7. Summary

We analyzed records of nine BBOBSs deployed by the TIARES project in the French Polynesia region. In addition to the isotropic V_{SV} model, we succeeded in estimating the intensity of azimuthal anisotropy at a depth range of ~20–100 km by combining ambient noise analysis at periods of 5–30 s and teleseismic wave analysis at periods of 30–200 s for the first time in the oceanic region. The isotropic shear wave model shows a large velocity reduction at a depth range of 40–80 km (Figure 3), where the lithosphere-asthenosphere boundary might exist. The azimuth of maximum *S* wave velocity was estimated to be NW–SE direction at depths of 20–100 km in both lithosphere and asthenosphere in this region. The direction is not perpendicular to the magnetic lineation but is almost parallel to the directions of plate motions during the age of seafloor spreading to the current age (Figure 7). This result indicates that the azimuthal anisotropy in the lithosphere records the plate motion during the age of seafloor spreading at least in our study area, which is different from the direction perpendicular to the ancient spreading axes, i.e., the current magnetic lineations. Spatial distribution of azimuthal anisotropy was estimated by shear wave splitting analysis. The result suggests the perturbation of azimuthal anisotropy caused by the current and ancient hot spot activities around the analyzed area. By comparing the intensity of anisotropy determined from surface waves and shear wave splitting times, we also estimated that the azimuthal anisotropy exists down to the depth of 190–210 km in the asthenosphere.

Acknowledgments

We thank Noriko Tada, Kiyoshi Baba, Takafumi Kasaya, and Natsue Abe for their help during the installation and recovery cruises. We are also thankful to Pierre Mery, Jean-Pierre Barriot, and Dominique Reymond for their logistic support in Tahiti. We are grateful to the associate editor and two anonymous reviewers for detailed comments that improved our manuscript significantly. This work was supported by grant-in-aids for JSPS Fellows (23-8157 and 26-847) and Scientific Research (19253004, 22000003, and 15K13558). We used GMT (Wessel and Smith 1991) and SAC2000 (Goldstein and Snoke 2005) software during this study. The BBOBS records of the TIARES project are distributed by Pacific21 (http://p21.jamstec.go.jp/). Any additional data may be obtained from the corresponding author (A. Takeo, akiko-t@eri.u-tokyo.ac.jp).

References

Adam, C., and A. Bonneville (2005), Extent of the South Pacific superswell, *J. Geophys. Res.*, *110*, B09408, doi:10.1029/2004JB003465.

Aki, K. (1957), Space and time spectra of stationary stochastic waves, with special reference to microtremors, *Bull. Earthquake Res. Inst.*, *35*(3), 415–456.

Aki, K., and K. Kaminuma (1963), Phase velocity of Love waves in Japan (Part 1): Love waves from the Aleutian shock of March 9, 1957, *Bull. Earthq. Res. Inst.*, *41*(1), 243–259.

Alvizuri, C., and T. Tanimoto (2011), Azimuthal anisotropy from array analysis of Rayleigh waves in Southern California, *Geophys. J. Int.*, *186*(3), 1135–1151, doi:10.1111/j.1365-246X.2011.05093.x.

Barruol, G. (2002), PLUME investigates South Pacific superswell, *Eos Trans. AGU*, *83*(45), 511, doi:10.1029/2002EO000354.

Barruol, G., D. Suetsugu, H. Shiobara, H. Sugioka, S. Tanaka, G. H. R. Bokelmann, F. R. Fontaine, and D. Reymond (2009), Mapping upper mantle flow beneath French Polynesia from broadband ocean bottom seismic observations, *Geophys. Res. Lett.*, *36*, L14301, doi:10.1029/2009GL038139.

Becker, T. W., S. Lebedev, and M. D. Long (2012), On the relationship between azimuthal anisotropy from shear wave splitting and surface wave tomography, *J. Geophys. Res.*, *117*, B01306, doi:10.1029/2011JB008705.

Becker, T. W., C. P. Conrad, A. J. Schaeffer, and S. Lebedev (2014), Origin of azimuthal seismic anisotropy in oceanic plates and mantle, *Earth Planet. Sci. Lett.*, *401*, 236–250, doi:10.1016/j.epsl.2014.06.014.

Behn, M. D., G. Hirth, and J. R. Elsenbeck II (2009), Implications of grain size evolution on the seismic structure of the oceanic upper mantle, *Earth Planet. Sci. Lett.*, *282*(1–4), 178–189, doi:10.1016/j.epsl.2009.03.014.

Burgos, G., J.-P. Montagner, E. Beucler, Y. Capdeville, A. Mocquet, and M. Drilleau (2014), Oceanic lithosphere-asthenosphere boundary from surface wave dispersion data, *J. Geophys. Res. Solid Earth*, *119*, 1079–1093, doi:10.1002/2013JB010528.

Cara, M., and J. J. Lévêque (1988), Anisotropy of the asthenosphere: The higher mode data of the Pacific revisited, *Geophys. Res. Lett.*, *15*(3), 205–208, doi:10.1029/GL015i003p00205.

Christensen, N. I., and M. H. Salisbury (1975), Structure and constitution of the lower oceanic crust, *Rev. Geophys.*, *13*(1), 57–86, doi:10.1029/RG013i001p00057.

Cox, H. (1973), Spatial correlation in arbitrary noise fields with application to ambient sea noise, *J. Acoust. Soc. Am.*, *54*(5), 1289–1301, doi:10.1121/1.1914426.

Crampin, S. (1982), Comments [on "Possible forms of seismic anisotropy of the uppermost mantle under oceans" by George E. Backus], *J. Geophys. Res.*, *87*(B6), 4636–4640, doi:10.1029/JB087iB06p04636.

Debayle, E., and Y. Ricard (2013), Seismic observations of large-scale deformation at the bottom of fast-moving plates, *Earth Planet. Sci. Lett.*, *376*, 165–177, doi:10.1016/j.epsl.2013.06.025.

Duncan, R., and I. McDougall (1976), Linear volcanism in French Polynesia, *J. Volcanol. Geotherm. Res.*, *1*(3), 197–227, doi:10.1016/0377-0273(76)90008-1.

Dunn, R. A., and D. R. Toomey (2001), Crack-induced seismic anisotropy in the oceanic crust across the East Pacific Rise (9°30'N), *Earth Planet. Sci. Lett.*, *189*(1–2), 9–17, doi:10.1016/S0012-821X(01)00353-3.

Dziewonski, A. M., and D. L. Anderson (1981), Preliminary reference Earth model, *Phys. Earth Planet. Inter.*, *25*(4), 297–356, doi:10.1016/0031-9201(81)90046-7.

Efron, B. (1979), Bootstrap methods: Another look at the jackknife, *Ann. Stat.*, *7*(1), 1–26, doi:10.1214/aos/1176344552.

Fontaine, F. R., G. Barruol, A. Tommasi, and G. H. R. Bokelmann (2007), Upper-mantle flow beneath French Polynesia from shear wave splitting, *Geophys. J. Int.*, *170*(3), 1262–1288, doi:10.1111/j.1365-246X.2007.03475.x.

Forsyth, D. W. (1975), The early structural evolution and anisotropy of the oceanic upper mantle, *Geophys. J. R. Astron. Soc.*, *43*(1), 103–162, doi:10.1111/j.1365-246X.1975.tb00630.x.

Forsyth, D. W., and A. Li (2005), Array analysis of two-dimensional variations in surface wave phase velocity and azimuthal anisotropy in the presence of multipathing interference, in *Seismol Earth Array Anal. Broadband Seism.*, edited by A. Levander and G. Nolet, pp. 81–97, AGU, Washington, D. C., doi:10.1029/157GM06.

Francis, T. J. G. (1969), Generation of seismic anisotropy in the upper mantle along the mid-oceanic ridges, *Nature*, *221*(5176), 162–165, doi:10.1038/221162b0.
French, S., V. Lekic, and B. Romanowicz (2013), Waveform tomography reveals channeled flow at the base of the oceanic asthenosphere, *Science*, *342*(6155), 227–230, doi:10.1126/science.1241514.
Gaherty, J. B., T. H. Jordan, and L. S. Gee (1996), Seismic structure of the upper mantle in a central Pacific corridor, *J. Geophys. Res.*, *101*(B10), 22,291–22,309, doi:10.1029/96JB01882.
Gaherty, J. B., D. Lizarralde, J. A. Collins, G. Hirth, and S. Kim (2004), Mantle deformation during slow seafloor spreading constrained by observations of seismic anisotropy in the western Atlantic, *Earth Planet. Sci. Lett.*, *228*(3–4), 255–265, doi:10.1016/j.epsl.2004.10.026.
Gripp, A. E., and R. G. Gordon (2002), Young tracks of hotspots and current plate velocities, *Geophys. J. Int.*, *150*(2), 321–361, doi:10.1046/j.1365-246X.2002.01627.x.
Harmon, N., D. Forsyth, and S. Webb (2007), Using ambient seismic noise to determine short-period phase velocities and shallow shear velocities in young oceanic lithosphere, *Bull. Seismol. Soc. Am.*, *97*(6), 2009–2023, doi:10.1785/0120070050.
Harmon, N., C. Rychert, and P. Gerstoft (2010), Distribution of noise sources for seismic interferometry, *Geophys. J. Int.*, *183*(3), 1470–1484, doi:10.1111/j.1365-246X.2010.04802.x.
Hess, H. H. (1964), Seismic anisotropy of the uppermost mantle under oceans, *Nature*, *203*(4945), 629–631, doi:10.1038/203629a0.
Ingber, L. (1989), Very fast simulated re-annealing, *Math. Comput. Model.*, *12*(8), 967–973, doi:10.1016/0895-7177(89)90202-1.
Isse, T., D. Suetsugu, H. Shiobara, H. Sugioka, K. Yoshizawa, T. Kanazawa, and Y. Fukao (2006), Shear wave speed structure beneath the South Pacific superswell using broadband data from ocean floor and islands, *Geophys. Res. Lett.*, *33*, L16303, doi:10.1029/2006GL026872.
Ito, G., M. McNutt, and R. L. Gibson (1995), Crustal structure of the Tuamotu Plateau, 15°S, and implications for its origin, *J. Geophys. Res.*, *100*(B5), 8097–8114, doi:10.1029/95JB00071.
Karato, S. (2012), On the origin of the asthenosphere, *Earth Planet. Sci. Lett.*, *321–322*, 95–103, doi:10.1016/j.epsl.2012.01.001.
Kawakatsu, H., P. Kumar, Y. Takei, M. Shinohara, T. Kanazawa, E. Araki, and K. Suyehiro (2009), Seismic evidence for sharp lithosphere-asthenosphere boundaries of oceanic plates, *Science*, *324*(5926), 499–502, doi:10.1126/science.1169499.
Kumar, P., and H. Kawakatsu (2011), Imaging the seismic lithosphere-asthenosphere boundary of the oceanic plate, *Geochem. Geophys. Geosyst.*, *12*, Q01006, doi:10.1029/2010GC003358.
Kumazawa, M., and O. L. Anderson (1969), Elastic moduli, pressure derivatives, and temperature derivatives of single-crystal olivine and single-crystal forsterite, *J. Geophys. Res.*, *74*(25), 5961–5972, doi:10.1029/JB074i025p05961.
Lizarralde, D., J. B. Gaherty, J. A. Collins, G. Hirth, and S. D. Kim (2004), Spreading-rate dependence of melt extraction at mid-ocean ridges from mantle seismic refraction data, *Nature*, *432*(7018), 744–747, doi:10.1038/nature03140.
Long, M. D., and R. D. van der Hilst (2005), Upper mantle anisotropy beneath Japan from shear wave splitting, *Phys. Earth Planet. Inter.*, *151*(3–4), 206–222, doi:10.1016/j.pepi.2005.03.003.
Lonsdale, P. (1988), Geography and history of the Louisville Hotspot Chain in the southwest Pacific, *J. Geophys. Res.*, *93*(B4), 3078–3104, doi:10.1029/JB093iB04p03078.
Maggi, A., E. Debayle, K. Priestley, and G. Barruol (2006a), Multimode surface waveform tomography of the Pacific Ocean: A closer look at the lithospheric cooling signature, *Geophys. J. Int.*, *166*(3), 1384–1397, doi:10.1111/j.1365-246X.2006.03037.x.
Maggi, A., E. Debayle, K. Priestley, and G. Barruol (2006b), Azimuthal anisotropy of the Pacific region, *Earth Planet. Sci. Lett.*, *250*(1–2), 53–71, doi:10.1016/j.epsl.2006.07.010.
Mainprice, D. (2007), Seismic anisotropy of the deep earth from a mineral and rock physics perspective, in *Treatese of Geophysics*, edited by G. Schubert, pp. 437–491, Elsevier, Amsterdam, doi:10.1016/B978-044452748-6.00045-6.
Marone, F., and B. Romanowicz (2007), The depth distribution of azimuthal anisotropy in the continental upper mantle, *Nature*, *447*(7141), 198–201, doi:10.1038/nature05742.
McNutt, M. K. (1998), Superswells, *Rev. Geophys.*, *36*(2), 211–244, doi:10.1029/98RG00255.
Montagner, J. (2002), Upper mantle low anisotropy channels below the Pacific Plate, *Earth Planet. Sci. Lett.*, *202*(2), 263–274, doi:10.1016/S0012-821X(02)00791-4.
Montagner, J.-P., and H.-C. Nataf (1986), A simple method for inverting the azimuthal anisotropy of surface waves, *J. Geophys. Res.*, *91*(B1), 511–520, doi:10.1029/JB091iB01p00511.
Montagner, J.-P., D.-A. Griot-Pommera, and J. Lavé (2000), How to relate body wave and surface wave anisotropy, *J. Geophys. Res.*, *105*(B8), 19,015, doi:10.1029/2000JB900015.
Monteiller, V., and S. Chevrot (2011), High-resolution imaging of the deep anisotropic structure of the San Andreas Fault system beneath southern California, *Geophys. J. Int.*, *186*(2), 418–446, doi:10.1111/j.1365-246X.2011.05082.x.
Müller, R. D., M. Sdrolias, C. Gaina, and W. R. Roest (2008), Age, spreading rates, and spreading asymmetry of the world's ocean crust, *Geochem. Geophys. Geosyst.*, *9*(4), Q04006, doi:10.1029/2007GC001743.
Nam, D., J.-S. Lee, and C. H. Park (2004), n-Dimensional cauchy neighbor generation for the fast simulated, *IEICE Trans. Inf. Syst.*, *E87-D*(11), 2499–2502.
Nettles, M., and A. M. Dziewonski (2008), Radially anisotropic shear velocity structure of the upper mantle globally and beneath North America, *J. Geophys. Res.*, *113*, B02303, doi:10.1029/2006JB004819.
Nishimura, C. E., and D. W. Forsyth (1989), The anisotropic structure of the upper mantle in the Pacific, *Geophys. J. Int.*, *96*(2), 203–229, doi:10.1111/j.1365-246X.1989.tb04446.x.
Patriat, M., F. Klingelhoefer, D. Aslanian, I. Contrucci, M. Gutscher, J. Talandier, F. Avedik, J. Francheteau, and W. Weigel (2002), Deep crustal structure of the Tuamotu plateau and Tahiti (French Polynesia) based on seismic refraction data — Art. no. 1656, *Geophys. Res. Lett.*, *29*(14), 1656, doi:10.1029/2001GL013913.
Raitt, R. W., G. G. Shor, T. J. G. Francis, and G. B. Morris (1969), Anisotropy of the Pacific upper mantle, *J. Geophys. Res.*, *74*(12), 3095–3109, doi:10.1029/JB074i012p03095.
Revenaugh, J., and T. H. Jordan (1991), Mantle layering from ScS reverberations: 2. The transition zone, *J. Geophys. Res.*, *96*(B12), 19,763–19,780, doi:10.1029/91JB01486.
Rychert, C. a., and P. M. Shearer (2011), Imaging the lithosphere-asthenosphere boundary beneath the Pacific using SS waveform modeling, *J. Geophys. Res.*, *116*, B07307, doi:10.1029/2010JB008070.
Saito, M. (1988), DISPER80: A subroutine package for the calculation of seismic normal-mode solutions, in *Seismological Algorithms: Computational Methods and Computer Programs*, pp. 293–319, Academic Press, San Diego, Calif.
Schlanger, S. O., M. O. Garcia, B. H. Keating, J. J. Naughton, W. W. Sager, J. A. Haggerty, J. A. Philpotts, and R. A. Duncan (1984), Geology and geochronology of the line islands, *J. Geophys. Res.*, *89*(B13), 11,261–11,272, doi:10.1029/JB089iB13p11261.
Schmerr, N. (2012), The Gutenberg discontinuity: Melt at the lithosphere-asthenosphere boundary, *Science*, *335*(6075), 1480–1483, doi:10.1126/science.1215433.

Seton, M., et al. (2012), Global continental and ocean basin reconstructions since 200Ma, *Earth Sci. Rev.*, *113*, 212–270, doi:10.1016/j.earscirev.2012.03.002.
Shinohara, M., T. Fukano, T. Kanazawa, E. Araki, K. Suyehiro, M. Mochizuki, K. Nakahigashi, T. Yamada, and K. Mochizuki (2008), Upper mantle and crustal seismic structure beneath the Northwestern Pacific Basin using a seafloor borehole broadband seismometer and ocean bottom seismometers, *Phys. Earth Planet. Inter.*, *170*(1–2), 95–106, doi:10.1016/j.pepi.2008.07.039.
Silver, P. G., and W. W. Chan (1991), Shear wave splitting and subcontinental mantle deformation, *J. Geophys. Res.*, *96*(B10), 16,429–16,454, doi:10.1029/91JB00899.
Smith, D. B., M. H. Ritzwoller, and N. M. Shapiro (2004), Stratification of anisotropy in the Pacific upper mantle, *J. Geophys. Res.*, *109*, B11309, doi:10.1029/2004JB003200.
Song, T.-R. A., and Y. Kim (2012), Anisotropic uppermost mantle in young subducted slab underplating Central Mexico, *Nat. Geosci.*, *5*(1), 55–59, doi:10.1038/ngeo1342.
Suetsugu, D., and H. Shiobara (2014), Broadband ocean-bottom seismology, *Annu. Rev. Earth Planet. Sci.*, *42*(1), 27–43, doi:10.1146/annurev-earth-060313-054818.
Suetsugu, D., et al. (2005), Probing South Pacific mantle plumes with ocean bottom seismographs, *Eos Trans. AGU*, *86*(44), 429–435, doi:10.1029/2005EO440001.
Suetsugu, D., T. Isse, S. Tanaka, M. Obayashi, H. Shiobara, H. Sugioka, T. Kanazawa, Y. Fukao, G. Barruol, and D. Reymond (2009), South Pacific mantle plumes imaged by seismic observation on islands and seafloor, *Geochem. Geophys. Geosyst.*, *10*, Q11014, doi:10.1029/2009GC002533.
Suetsugu, D., H. Shiobara, H. Sugioka, A. Ito, T. Isse, T. Kasaya, and N. Tada (2012), TIARES Project—Tomographic investigation by seafloor array experiment for the Society hotspot, *Earth Planets Space*, *64*(4), i–iv, doi:10.5047/eps.2011.11.002.
Szu, H., and R. Hartley (1987), Fast simulated annealing, *Phys. Lett. A*, *122*(3–4), 157–162, doi:10.1016/0375-9601(87)90796-1.
Takeo, A., K. Nishida, T. Isse, H. Kawakatsu, H. Shiobara, H. Sugioka, and T. Kanazawa (2013), Radially anisotropic structure beneath the Shikoku Basin from broadband surface wave analysis of ocean bottom seismometer records, *J. Geophys. Res. Solid Earth*, *118*, 2878–2892, doi:10.1002/jgrb.50219.
Takeo, A., D. W. Forsyth, D. S. Weeraratne, and K. Nishida (2014), Estimation of azimuthal anisotropy in the NW Pacific from seismic ambient noise in seafloor records, *Geophys. J. Int.*, *199*(1), 11–22, doi:10.1093/gji/ggu240.
Takeuchi, H., and M. Saito (1972), Seismic surface waves, in *Methods in Computational Physics*, edited by B. A. Bolt, pp. 217–295, Academic Press, New York.
Tanimoto, T., and D. L. Anderson (1984), Mapping convection in the mantle, *Geophys. Res. Lett.*, *11*(4), 287–290, doi:10.1029/GL011i004p00287.
Toomey, D. R., D. Jousselin, R. A. Dunn, W. S. D. Wilcock, and R. S. Detrick (2007), Skew of mantle upwelling beneath the East Pacific Rise governs segmentation, *Nature*, *446*(7134), 409–414, doi:10.1038/nature05679.
Weaver, R., B. Froment, and M. Campillo (2009), On the correlation of non-isotropically distributed ballistic scalar diffuse waves, *J. Acoust. Soc. Am.*, *126*(4), 1817–1826, doi:10.1121/1.3203359.
Wolfe, C. J., and P. G. Silver (1998), Seismic anisotropy of oceanic upper mantle: Shear wave splitting methodologies and observations, *J. Geophys. Res.*, *103*(B1), 749–771, doi:10.1029/97JB02023.
Yao, H., P. Gouédard, J. A. Collins, J. J. McGuire, and R. D. van der Hilst (2011), Structure of young East Pacific Rise lithosphere from ambient noise correlation analysis of fundamental- and higher-mode Scholte-Rayleigh waves, *C. R. Geosci.*, *343*, 571–583, doi:10.1016/j.crte.2011.04.004.
Yoshizawa, K., and B. L. N. Kennett (2015), The lithosphere-asthenosphere transition and radial anisotropy beneath the Australian continent, *Geophys. Res. Lett.*, *42*, 3839–3846, doi:10.1002/2015GL063845.
Yuan, K., and C. Beghein (2013), Seismic anisotropy changes across upper mantle phase transitions, *Earth Planet. Sci. Lett.*, *374*, 132–144, doi:10.1016/j.epsl.2013.05.031.